

# UCLA

## UCLA Previously Published Works

### Title

ZeroCAL: Eliminating Carbon Dioxide Emissions from Limestones Decomposition to Decarbonize Cement Production.

### Permalink

<https://escholarship.org/uc/item/2qk5w2r8>

### Journal

ACS Sustainable Chemistry and Engineering, 12(43)

### ISSN

2168-0485

### Authors

Leão, Adriano  
Collin, Marie  
Ghodkhande, Swarali  
et al.

### Publication Date

2024-10-28

### DOI

10.1021/acssuschemeng.4c03193

Peer reviewed

# ZeroCAL: Eliminating Carbon Dioxide Emissions from Limestone's Decomposition to Decarbonize Cement Production

Adriano Leão,<sup>#</sup> Marie Collin,<sup>#</sup> Swarali Ghodkhande, Arnaud Bouissonnié, Xin Chen, Benjamin Malin, Yiming Liu, Geanna Hovey, Jagannathan Govindhakannan, Erika La Plante, David Jassby, Torben Gädt, Lorenzo Corsini, Dante Simonetti, Fabian Rosner, and Gaurav Sant<sup>\*</sup>



Cite This: *ACS Sustainable Chem. Eng.* 2024, 12, 15762–15787



Read Online

ACCESS |

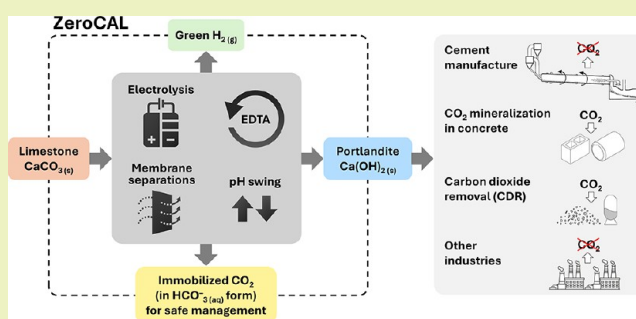
Metrics & More

Article Recommendations

**ABSTRACT:** Limestone (calcite,  $\text{CaCO}_3$ ) is an abundant and cost-effective source of calcium oxide (CaO) for cement and lime production. However, the thermochemical decomposition of limestone ( $\sim 800\text{ }^\circ\text{C}$ , 1 bar) to produce lime (CaO) results in substantial carbon dioxide ( $\text{CO}_2(\text{g})$ ) emissions and energy use, i.e.,  $\sim 1$  tonne [t] of  $\text{CO}_2$  and  $\sim 1.4$  MWh per t of CaO produced. Here, we describe a new pathway to use  $\text{CaCO}_3$  as a Ca source to make hydrated lime (portlandite,  $\text{Ca}(\text{OH})_2$ ) at ambient conditions ( $p$ ,  $T$ )—while nearly eliminating process  $\text{CO}_2(\text{g})$  emissions (as low as 1.5 mol. % of the  $\text{CO}_2$  in the precursor  $\text{CaCO}_3$ , equivalent to 9 kg of  $\text{CO}_2(\text{g})$  per t of  $\text{Ca}(\text{OH})_2$ )—within an aqueous flow-electrolysis/pH-swing process that coproduces hydrogen ( $\text{H}_2(\text{g})$ ) and oxygen ( $\text{O}_2(\text{g})$ ).

Because  $\text{Ca}(\text{OH})_2$  is a zero-carbon precursor for cement and lime production, this approach represents a significant advancement in the production of zero-carbon cement. The **Zero Carbon Lime (ZeroCAL)** process includes dissolution, separation/recovery, and electrolysis stages according to the following steps: (Step 1) chelator (e.g., ethylenediaminetetraacetic acid, EDTA)-promoted dissolution of  $\text{CaCO}_3$  and complexation of  $\text{Ca}^{2+}$  under basic ( $>\text{pH } 9$ ) conditions, (Step 2a) Ca enrichment and separation using nanofiltration (NF), which allows separation of the Ca-EDTA complex from the accompanying bicarbonate ( $\text{HCO}_3^-$ ) species, (Step 2b) acidity-promoted decomplexation of Ca from EDTA, which allows near-complete chelator recovery and the formation of a Ca-enriched stream, and (Step 3) rapid precipitation of  $\text{Ca}(\text{OH})_2$  from the Ca-enriched stream using electrolytically produced alkalinity. These reactions can be conducted in a seawater matrix yielding coproducts including hydrochloric acid (HCl) and sodium bicarbonate ( $\text{NaHCO}_3$ ), resulting from electrolysis and limestone dissolution, respectively. Careful analysis of the reaction stoichiometries and energy balances indicates that approximately 1.35 t of  $\text{CaCO}_3$ , 1.09 t of water, 0.79 t of sodium chloride (NaCl), and  $\sim 2$  MWh of electrical energy are required to produce 1 t of  $\text{Ca}(\text{OH})_2$ , with significant opportunity for process intensification. This approach has major implications for decarbonizing cement production within a paradigm that emphasizes the use of existing cement plants and electrification of industrial operations, while also creating approaches for alkalinity production that enable cost-effective and scalable  $\text{CO}_2$  mineralization via  $\text{Ca}(\text{OH})_2$  carbonation.

**KEYWORDS:** limestone, cement, decarbonization, electrolysis, pH swing



## 1. INTRODUCTION AND BACKGROUND

Concrete is the second most used material globally after water.<sup>1</sup> However, the production of cement (Portland Cement, PC), the binding agent in concrete, results in  $\sim 1$  tonne [t] of  $\text{CO}_2$  emitted per t of PC produced. The *direct*  $\text{CO}_2$  emissions derive  $\sim 60\%$  from the thermochemical decomposition of  $\text{CaCO}_3$  to produce CaO (“process emissions”, eq 1) and  $\sim 40\%$  from the combustion of fossil fuels to heat the kiln to  $\sim 1500\text{ }^\circ\text{C}$  (“combustion emissions”) to ensure the clinkering reactions<sup>2,3</sup> typically requiring  $>1$  MWh of thermal energy per t of CaO produced.<sup>4–7</sup> Additionally, typical cement plant operations require  $\sim 10\%$  of electrical energy input<sup>8–11</sup> that contribute  $\sim 10\%$  of

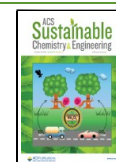
indirect  $\text{CO}_2$  emissions.<sup>12</sup> As a consequence, the annual global production of  $\sim 4.5$  billion t of PC—from an installed capital asset base of  $>\$400$  billion including cement plants, adjacent limestone quarries, transport infrastructure, etc.—results in 8–10% of anthropogenic  $\text{CO}_2$  emissions.<sup>13,14</sup>

**Received:** April 30, 2024

**Revised:** September 14, 2024

**Accepted:** September 17, 2024

**Published:** October 10, 2024



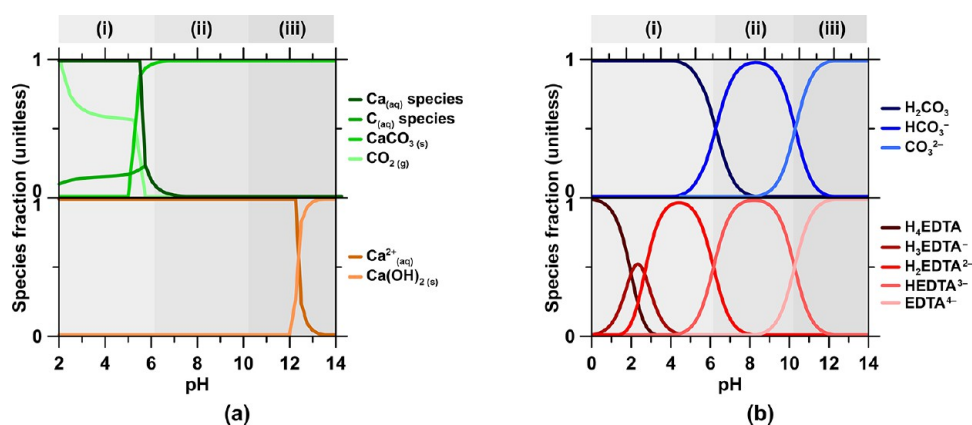
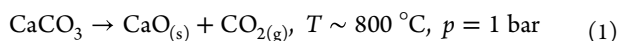


**Figure 1.** Speciation, in aqueous solution at 25 °C and 1 bar, of (a)  $\text{CaCO}_3$  and  $\text{Ca}(\text{OH})_2$  and (b) Dissolved Inorganic Carbon (DIC) and EDTA. For reference, the limiting solubilities of  $\text{CaCO}_3$ ,  $\text{CO}_2$ , and EDTA in water at pH 7 are  $\sim 4.0$ ,  $\sim 0.1$ , and  $\sim 420$  mmol/L, respectively.

Unfortunately, decarbonizing the heat source alone, e.g., through renewable heat, is insufficient to decarbonize PC production and currently supply constrained by the availability of renewable energy.<sup>15</sup> Rather, decarbonizing the existing thermochemical paradigm of PC production requires the replacement, displacement, or the transformation of limestone as the CaO source.



Because PC accounts for  $\sim 90\%$  of the global warming potential (GWP) of concrete, substantial efforts have been directed toward replacing PC with supplementary cementitious materials such as fly ash, slag, calcined clays, etc. in the binder fraction of concrete.<sup>12</sup> However, this practice of “dilution”, which does reduce the PC content of the concrete binder, does not alter the embodied carbon intensity—direct  $\text{CO}_2$  emissions—of PC/clinker production at the site and scale of a cement plant. Thus, it is not a means for decarbonizing PC production. While carbon capture and (geological) storage (CCS) is being extensively suggested as a pathway for PC decarbonization, the costs of (i) deploying carbon capture systems at typical “million tonne per annum” (MTPA) scale cement plants, CapEx  $\sim$  \$1 billion, (ii) pipeline transport of compressed  $\text{CO}_2$ , and (iii) injection and monitoring of injected  $\text{CO}_2$  in sequestration sites implies that CCS will cost well over  $\$120/\text{t}_{\text{CO}_2}$  and, thus nearly double the price of PC.<sup>15</sup> Finally, after a century of industrial operations, state-of-the-art PC plants fitted with the Best Available Technologies (BATs), such as heat recovery systems and kiln insulation, are operating close to the limits of practical efficiencies.<sup>8–11</sup> Thus, only marginal improvements in these systems can be realized. This indicates that actual decarbonization of PC production requires the displacement of thermochemical routes that decompose limestone into CaO as implied by the today’s manufacturing paradigm.

Given the well-established complexities of decarbonizing PC production, two approaches have gained prominence. First, electrochemical “electron-to-molecule” approaches focus on producing an alternate cement chemistry that offers performance but not compositional equivalence to PC.<sup>16,17</sup> Second, alternative feedstock and manufacturing processes that produce a traditional PC.<sup>18,19</sup> What ties both of these, and related approaches, is that they make use of non-carbonate Ca-containing feedstocks (e.g., steel slags, fly

ashes, basalts, etc.) to avoid  $\text{CO}_2$  emissions.<sup>16,18,19</sup> While promising, these approaches face major challenges. For example, feedstocks such as slags and fly ashes are supply constrained in comparison to the scale of PC production,<sup>20,21</sup> while basalts, although not supply constrained, are far more difficult to extract alkaline metals from as compared with carbonate rocks such as limestone.<sup>22</sup> On the other hand, many newer approaches imply a higher risk of stranding existing cement plants because of a need for different raw materials and/or different process trains,<sup>23</sup> thus requiring the buildout of new green-field facilities,<sup>15</sup> a financially challenging proposition when seen from the perspective of the existing industry. *This raises the question if/how the unit economics of decarbonized cement could achieve net present value (NPV) parity as compared to PC manufactured today?*

To address these challenges, this paper suggests a transformative near process- $\text{CO}_2$ -emissions-free pathway that makes use of limestone within an aqueous electrochemical paradigm to produce portlandite ( $\text{Ca}(\text{OH})_2$ )—a “drop in” zero-carbon feedstock for PC production. Here, the portlandite is introduced at an intermediate stage between limestone quarrying and the clinkering steps. Not only does this approach obviate the need for CCS for cement/lime decarbonization but, importantly, via the production of green hydrogen (and oxygen) it also provides (partial) clean energy for high-grade cement kiln heating or cogeneration. Taken together, the proposed ZeroCAL (Zero Carbon Lime) approach allows us to define cost-effective, accessible, and scalable electrified solutions for cement decarbonization at the site and scale of existing cement plants without resorting to CCS as the only pathway for cement (clinker) decarbonization.

## 2. NEW CONCEPT: THE ZeroCAL PROCESS

Calcium carbonate polymorphs such as calcite, aragonite, and vaterite, as well as rocks composed thereof, e.g., limestone, present an abundant source of CaO. However, under thermal activation, limestone decomposes to release its mineralized  $\text{CO}_2$ . While under circumneutral-to-alkaline aqueous conditions ( $\text{pH} > 6$ ; Figure 1a), limestone can be dissolved with virtually zero  $\text{CO}_{2(g)}$  emission, its dissolution rate in this regime is very slow:  $\sim 5 \times 10^{-6}$  mol/ $\text{m}^2/\text{s}$ .<sup>24</sup> Furthermore, the low solubility of limestone under these conditions, 25.5 mmol/L at pH 6 to 0.1 mmol/L at pH

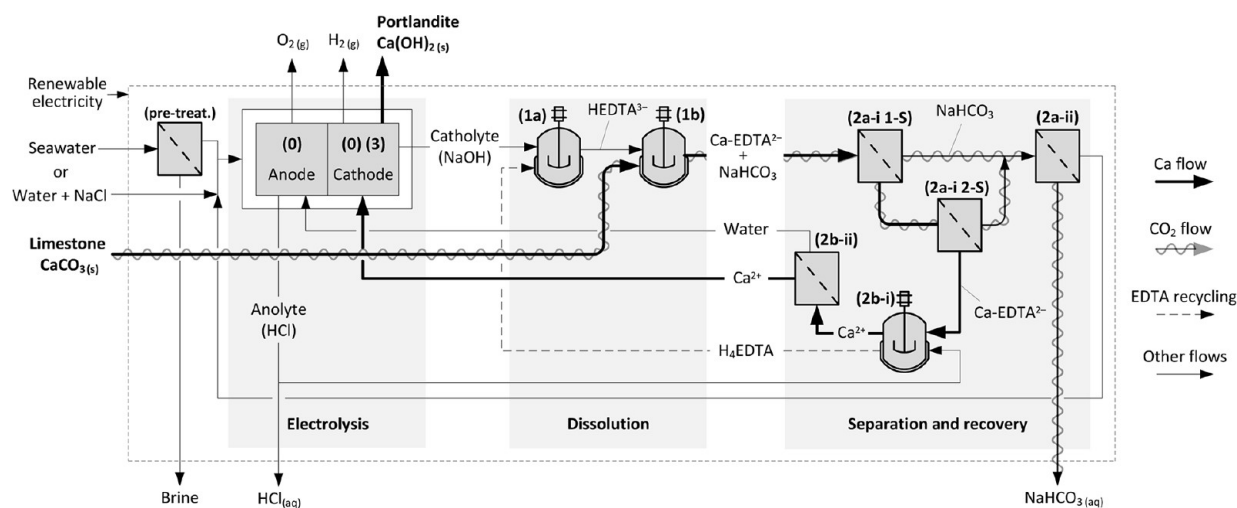


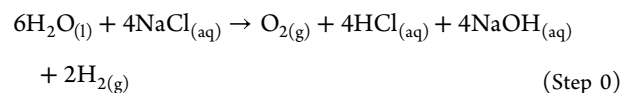
Figure 2. Representative process flow diagram (PFD) of the ZeroCAL process showing the different unit operations and materials flows.

10,<sup>24</sup> implies an enormous water demand for Ca mobilization by ordinary dissolution. While the dissolution rates and the Ca capacity of the solution greatly increase with decreasing pH, the speciation change of dissolved inorganic carbon (DIC)—as disclosed by the Bjerrum diagram (Figure 1b)—from dominantly bicarbonate ( $\text{HCO}_3^-$ ) and/or carbonate ( $\text{CO}_3^{2-}$ ) anions at pH > 6<sup>25,26</sup> to carbonic acid ( $\text{H}_2\text{CO}_3$ ) and  $\text{CO}_{2(g)}$  implies the undesirable and substantial emission of  $\text{CO}_2$  with decreasing pH.<sup>27,28</sup>

Thus, a potential approach for effective aqueous Ca mobilization from  $\text{CaCO}_3$  and the subsequent use of this Ca for PC production implies enhancing the apparent solubility of limestone at alkaline pH. This can be achieved by making one or more dissolved solute species (e.g., of  $\text{CaCO}_3$ :  $\text{Ca}^{2+}$ ,  $\text{CO}_3^{2-}$ , and/or  $\text{HCO}_3^-$ ) inconsequential in terms of affecting the undersaturation, thereby enhancing the dissolution rate and solubility, without inducing the reprecipitation of  $\text{CaCO}_3$ . The ZeroCAL approach relies on the use of chelating agents such as ethylenediaminetetraacetic acid (EDTA)<sup>29–31</sup> that enhance the dissolution rate of  $\text{CaCO}_3$  and the Ca bearing capacity of solutions via an *apparent solubility increase* mechanism.<sup>32–34</sup> Based on this reasoning, the process encompasses the following steps (Steps 0–3, Figure 2).

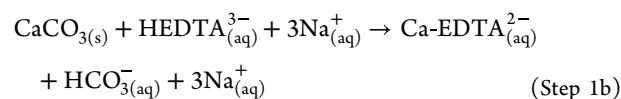
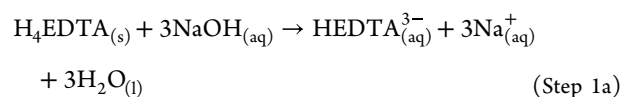
**(Step 0)** This involves the electrochemical production of acid (HCl), base (NaOH), oxygen ( $\text{O}_{2(g)}$ ), and hydrogen ( $\text{H}_{2(g)}$ ), by the electrolysis of a salt-in-water (NaCl; ~ 0.5 mol/L; e.g., seawater) electrolyte using proprietary oxygen-selective anodes (OSAs) with >98 mol. % selectivity for oxygen evolution.<sup>35,36</sup> The electrolysis step ensures that there is no extrinsic need for stoichiometric additives to induce a pH-swing. It should be noted that, while here NaCl is implicated as a low-cost, abundant, high-conductivity electrolyte, e.g., by using softened seawater<sup>37</sup> as a reaction medium and electrolyte, it is only a viable option if  $\text{Cl}_{2(g)}$  evolution during electrolysis can be suppressed. On the other hand, if the electrolyte were maintained in a closed-loop by recirculating flow, it would be possible to use stable non-oxidizing salt-in-water electrolytes such as  $\text{NaClO}_4$  and typical platinum-based anodes or other suitable catalysts, without the need for OSAs. The general electrolytic reaction

may be written as follows (refer to Section A1.1 in the Appendix for details):

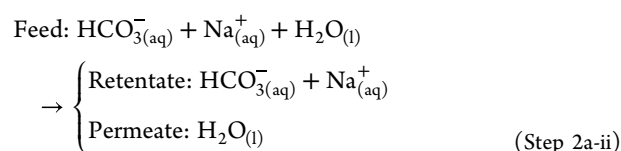
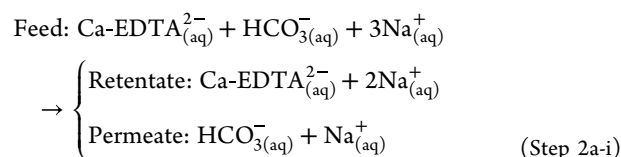


Note that, during the subsequent Steps 1–3, 5 mol of NaOH and 4 mol of HCl are required per mol of  $\text{Ca}(\text{OH})_2$  produced, meaning that a multiplier of 5/4 needs to be applied to Step 0 to describe the overall reaction. Here, all of the acid and base needed is produced electrolytically, and *in situ*, ensuring that no external additives are needed for the ZeroCAL process.

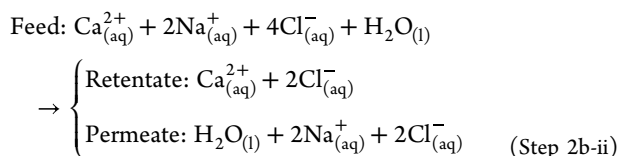
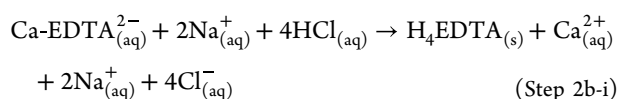
**(Step 1)** For valence compensation, EDTA dissolution requires 1 mol of NaOH per  $\text{H}^+$  released from the initially dissolved  $\text{H}_4\text{EDTA}$  species, i.e., 3 mol of NaOH to form  $\text{HEDTA}^{3-}$  at pH 9 (Figure 1b). EDTA then promotes the dissolution of  $\text{CaCO}_3$ , and the complexation of Ca cations under basic conditions:



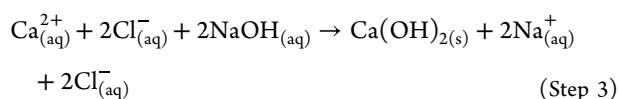
**(Step 2a)** Ca enrichment and separation using nano-filtration (NF) allows separation of the Ca-EDTA complex from the accompanying bicarbonate ( $\text{HCO}_3^-$ ) anions:



(Step 2b) The acid produced allows the decomplexation of Ca from EDTA which allows near-complete chelator recovery, and the formation of a Ca-enriched feed solution:

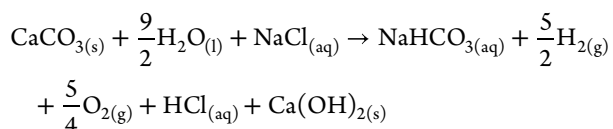


(Step 3) This involves the rapid precipitation of Ca(OH)<sub>2</sub> within the catholyte of a flow electrolyzer:

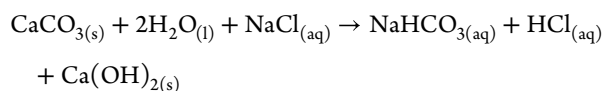


**(Overall reaction)** Calcium carbonate, water, and the electrolyte as acid–base conjugates are transformed with the aid of the (recycled) chelating agent into aqueous sodium bicarbonate/carbonate—as determined by the dissolution pH, here simplified to NaHCO<sub>3</sub>—for recovery/utilization or for durable storage, and coproducts including hydrogen and oxygen (gases), hydrochloric acid (liquid), and calcium hydroxide (solid). The overall reaction can be decomposed into two reactions: (i) the dissolution–precipitation reaction and (ii) the water-splitting reaction as follows:

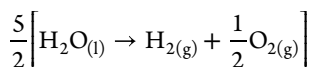
**Overall reaction:**



**Dissolution–precipitation reaction:**



**Water-splitting reaction:**



Herein, deprotonated EDTA (HEDTA<sup>3-</sup>; Figure 1 and Step 1a) is used to enhance the dissolution rate and apparent solubility of CaCO<sub>3</sub> at pH > 7. While this example emphasizes EDTA, it is only one of many possible chelating agents that could be used. The hexadentate structure of EDTA consists of four carboxylate and two amine groups with the general formula [CH<sub>2</sub>N(CH<sub>2</sub>CO<sub>2</sub>H)<sub>2</sub>]<sub>2</sub>. In general, the metal-chelation capacity and stability increase with pH.<sup>29,31</sup> CaCO<sub>3</sub> dissolution is enhanced by EDTA at ambient temperature and pressure, thereby promoting the Ca-complexation reaction in Step 1b and Figure 1. In the presence of Ca species in aqueous solution, the binding affinity of EDTA ensures that the deprotonated chelator rearranges around the Ca<sup>2+</sup> cation extracted from the CaCO<sub>3</sub> lattice through a surface chelation reaction.<sup>32,33</sup> Thus, Ca species are adsorbed onto the binding sites of EDTA resulting in the formation of a monocalcium-EDTA (Ca-

EDTA<sup>2-</sup>) complex at the calcite/liquid interface, while the liberated H<sup>+</sup> protonates the CO<sub>3</sub><sup>2-</sup> species that is released alongside the Ca<sup>2+</sup> cation into its bicarbonate form (HCO<sub>3</sub><sup>-</sup>).<sup>32,33,38</sup> This reaction sequence is well-known and in an alkaline environment prevents degassing of CO<sub>2</sub>. Experimental evidence and optimal conditions for such are reported in Section 4.1.

Pressure-driven membrane technology has become increasingly prevalent, notably NF due to its unique properties: tailored selectivity, lower pressure, higher flow rates, and lower investment and operating costs vis-à-vis well-established (seawater) reverse osmosis (RO).<sup>39</sup> Although new applications require demonstration of technical outcomes and commercial viability at industrial scale, successful and cost-effective commercial applications of NF processes have been reported across various fields.<sup>40–47</sup> NF membranes allow for the steric (size exclusion) and charge rejection of large molecules (>100 Da)<sup>48</sup> such as metal-chelator complexes.<sup>49,50</sup> The NF-based separation of such complexes from monovalent species has been reported.<sup>51</sup> Modern membranes allow tailored applications via: (i) hydrophilic surface functional groups that enhance water permeability while preventing scaling,<sup>52</sup> (ii) a large-pore matrix for high water flux and monovalent ion permeability,<sup>53</sup> while electrostatic interactions retain the charged complexes, and (iii) control of the state of membrane surface charge<sup>54</sup> resulting in high monovalent and low multivalent permeance due to Donnan and dielectric solvation-energy barrier mechanisms.<sup>55,56</sup> Here, combining chelator-aided dissolution with NF enables the production of a Ca-rich stream that can be used to electrochemically produce portlandite using a CaCO<sub>3</sub> feedstock. The complexation of calcium (Ca = 40.08 Da) by EDTA yields a relatively large molecular complex (Ca-EDTA complex mass = 332.30 Da), which is ~8 times larger than Ca cations, with a negative divalent charge. Thus, dialytic (i.e., pressure-driven) NF membranes can be used to selectively retain and concentrate Ca species and separate CO<sub>2</sub> species via size exclusion, electrostatic, and/or surface interactions.<sup>57,58</sup> In particular, for the Ca-EDTA/Na-HCO<sub>3</sub> separation (Step 2a-i), it is desirable to achieve high rejection of the Ca-EDTA complex and high monovalent (HCO<sub>3</sub><sup>-</sup>) ion permeation. For the NaHCO<sub>3</sub>/water separation (Step 2a-ii) and Ca enrichment (Step 2a-iii), high monovalent rejection and high divalent ion rejection, respectively, are desired. In all cases, a high membrane flux, ~10 L/(m<sup>2</sup>·h·bar), is desired for high-liquid throughput and low energy processing, ~1 kWh/m<sup>3</sup>.

Following Ca-EDTA recovery, electrolytically produced HCl (Step 0) is used for dechelation, i.e., to promote tetraprotonation of EDTA resulting in the formation/precipitation of its insoluble H<sub>4</sub>EDTA variant. This results in the release and accumulation of Ca cations in an acidic solution with Cl<sup>-</sup> as the balancing anion. The EDTA precipitates can be separated from the decomplexed and now solvated/mobile Ca<sup>2+</sup> cations (Step 2b-i), which can be further enriched using NF (Step 2b-ii).<sup>59–61</sup> The 20 mol. % stoichiometric excess of electrolytically produced HCl (see the Step 0 and Step 2b-i equations) can be neutralized by the controlled dissolution of abundant Ca- and/or Mg-bearing rocks.<sup>35,36</sup> Hereafter, the Ca-enriched solution is electrolytically alkalized (Step 0) to pH > 12 to rapidly precipitate Ca(OH)<sub>2</sub> at ambient conditions (Figure 1a, Step 3). With progressive alkalization, precipitation continues so

long as the ion activity product (IAP) of  $\text{Ca}(\text{OH})_2$  exceeds its solubility product ( $K_{\text{sp}}$ ); i.e., the logarithm of the saturation index (SI) exceeds zero:  $\text{SI} = \log[\text{IAP}/K_{\text{sp}}]$ , where for  $\text{Ca}(\text{OH})_2$ ,  $\text{IAP} = \{\text{Ca}^{2+}\}\{\text{OH}^{-}\}^2$ , where  $\{\}$  indicate ion activities and  $K_{\text{sp}} = 5.2 \times 10^{-6}$  at  $p = 1$  bar and  $T = 25$  °C.<sup>62</sup> The supply of alkalinity is ensured via electrolytic hydrogen evolution reaction (HER)<sup>35,63</sup> at the cathode, and so long as the hydroxyl ion ( $\text{OH}^{-}$ ) generation rate and the rate of Ca supply maintain supersaturated conditions,  $\text{Ca}(\text{OH})_2$  precipitation occurs continuously. In the following sections, special focus is paid to describe the nonelectrolysis Steps 1–3, as these represent the unique process innovations that underlie the ZeroCAL process.

### 3. MATERIALS AND METHODS

Unless specified, all experimental data imply at least triplicate measurements, and hence the mean and standard deviations were derived for all data points. All stoichiometries and mass, charge (Table A1 in the Appendix), and energy balances were validated experimentally. All product streams from each discrete step of the process were used in subsequent steps to establish process integration.

**3.1. Materials. Solids.** Two calcium precursors were used: an analytical reagent (AR)-grade calcite sample (>99 mass %) and a high-purity limestone rock. The AR calcite was used as received. The limestone rock was ground to a fine powder in a planetary ball mill and sieved to between 30 and 90  $\mu\text{m}$  to retrieve a particle size distribution (PSD) similar to that of the AR calcite. Both samples were fully characterized, as described below. The results are summarized in Table 1.

**Solutions.** Solid  $\text{H}_4\text{EDTA}$  powder (>99 mass%) and solid NaOH powder (>99 mass%) were used as received to prepare EDTA-containing solutions. Unless specified, all

**Table 1. Characterization of the AR Calcite and Limestone Samples<sup>a</sup>**

	Particle Size Distribution				SSA ( $\text{cm}^2/\text{g}$ )		
	$d_{10}$ ( $\mu\text{m}$ )	$d_{50}$ ( $\mu\text{m}$ )	$d_{90}$ ( $\mu\text{m}$ )				
AR calcite	22.9	39.5	67.9		0.028		
limestone	5.9	21.4	72.4		0.023		
	Oxide Content (mass %)						
	XRF					TGA	
	CaO	MgO	SiO <sub>2</sub>	Al <sub>2</sub> O <sub>3</sub>	Fe <sub>2</sub> O <sub>3</sub>	others	
AR calcite	>55.8					<0.1	44.1
limestone	57.7	0.6	1.4	0.4	0.2	<0.1	39.7
	Mineral Content (mass %)						
	calcite ( $\text{CaCO}_3$ )	dolomite [ $\text{CaMg}(\text{CO}_3)_2$ ]	quartz ( $\text{SiO}_2$ )				
AR calcite	100.0						
limestone	96.7		1.8			1.5	

<sup>a</sup>The PSD from light scattering analysis, the bulk oxide composition from XRF analysis and TGA, and the mineral composition from XRD analysis are provided.

solutions were prepared with 18 M $\Omega$ -cm Milli-Q water (MQW). In some instances, NaCl-containing MQW or simulated seawater (“Instant Ocean Seawater: IOSw”) were used instead of pure MQW.

**Membranes.** Eight commercial NF membranes were selected for screening for separation Steps 2-i, 2-ii, and 2-

iii based on common performance parameters, i.e., the normalized permeate flux and observed rejections (Table 2).

**3.2. Solid-Phase Analysis. Particle Size Distribution.** The PSD of the solids was measured by light scattering from dilute suspensions of the powders in water using a Beckman Coulter LS13-320 light scattering analyzer. The uncertainty in the light scattering analysis was estimated to be ~10% based on three measurements and assuming the density of both samples to be that of pure calcite, i.e., 2.711  $\text{g}/\text{cm}^3$ . In addition, the PSD was used to estimate the specific surface area (SSA, in  $\text{cm}^2/\text{g}$ ) of the samples.

**X-ray Fluorescence.** X-ray fluorescence (XRF) was conducted using a Hitachi X-Supreme8000 series XRF analyzer under helium (He) flow. The sample holders were double cleaned with isopropyl alcohol (IPA) prior to use. The solid (powder) sample was packed into the sample holder until “infinite” thickness condition (i.e., >2 mm) was achieved. The He flow was maintained below 10 psi and maximum tube current maintained at <30 kW during the analysis.

**Thermogravimetric Analysis.** Thermogravimetric analysis (TGA) was performed using a PerkinElmer STA 8000 analyzer under a flow of ultrapure nitrogen in aluminum oxide crucibles. A heating ramp of 10 °C/min was used between 35 and 950 °C, after 5 min of equilibration at 35 °C.

**X-ray Diffraction.** X-ray diffraction (XRD) analysis was performed using a PANalytical X’PertPro diffractometer ( $\theta$ – $\theta$  configuration, Cu  $K\alpha$  radiation, and  $\alpha = 1.54$  Å) on powdered samples. The scans were acquired between 5° and 70° with a step size of 0.02° using a X’Celerator 2 detector. Rietveld refinement of the samples was performed using Profex and BGMN packages.<sup>73–75</sup>

**Fourier Transform Infrared Spectroscopy.** Solid-state attenuated-total-reflection Fourier transform infrared spectroscopy (ATR-FTIR) was performed using a PerkinElmer Spectrum Two FT-IR spectrometer. The powdered samples were pressed using around 90 N of force onto a diamond/ZnSe composite crystal to ensure good contact and generate total internal reflection. The spectra reported herein were obtained by averaging 4 scans over the wavenumber range of 4000–400  $\text{cm}^{-1}$  at a resolution of 1  $\text{cm}^{-1}$ .

**3.3. Solution-Phase Analysis. Inductively Coupled Plasma Optical Emission Spectrometry.** Inductively coupled plasma optical emission spectrometry (ICP-OES) was performed using a PerkinElmer Avio 200 analyzer for multi-elemental analysis to quantify Ca and Na concentrations in solution (i.e., in a 5 vol % trace-metal-grade  $\text{HNO}_3$  matrix). All intensity measurements, measured in radial view, were converted to concentration units using a calibration curve with a blank and 7 calibration points between 0.1 and 25 ppm, prepared using standard solutions (1000 ppm Inorganic Ventures). Our testing showed that the presence of trace amounts of EDTA in the samples prepared for ICP measurement does not affect the intensity reading. Note that, for the limestone sample, Mg, Fe, and Al, as elements that can all complex with EDTA, were analyzed in a following a similar method as that used for Ca analysis. In general, for both feedstocks, Mg was found to be present in trace amounts (i.e., <1 mmol/L that corresponds to <1 mol. % of the amount of Ca in solution) while Al and Fe were below the detection limit.

**Table 2. Attributes of the NF Membranes Including the Nominal Pore Size, Pure Water Normalized Flux, and Divalent and Monovalent Salt Rejections**

membrane type	membrane pore size (10 <sup>2</sup> Da)	water permeability (L/m <sup>2</sup> ·h·bar)	salt rejection (%)	producer/material	reference
NF90	2	8.9	99, MgSO <sub>4</sub> ; 93, NaCl	FilmTec/polyamide	Dupont, <sup>64</sup> Ramdani <sup>65</sup>
TS40	2	4.5	90, MgSO <sub>4</sub> ; 50, NaCl	Trisep/polypiperazine	Trisep <sup>66</sup>
NF270	3	11.0	97, MgSO <sub>4</sub> ; 50, NaCl	FilmTec/polypiperazine	Dupont, <sup>67</sup> Ramdani <sup>65</sup>
NFW	4	10.6	97, MgSO <sub>4</sub> ; 20, NaCl	Synder/polyamide	Synder <sup>68</sup>
XN45	5	7.8	95, MgSO <sub>4</sub> ; 20, NaCl	Trisep/polypiperazine	Trisep <sup>69</sup>
TS80	1.5	8.6	99, MgSO <sub>4</sub> ; 80, NaCl	Trisep/polyamide	Trisep <sup>70</sup>
SB90	1.5	3.7	97, MgSO <sub>4</sub> ; 85, NaCl	Trisep/cellulose acetate	Trisep <sup>71</sup>
NP030	5	>1.0	N.D., MgSO <sub>4</sub> ; 86, NaCl	Microdyn Nadir/poly(ether sulfone)	Nadir <sup>72</sup>

**Titration.** Volumetric titrations were performed using an OrionStar T910 instrument and using HCl as the titrant to determine the concentration of dissolved EDTA, Ca-EDTA complex, and DIC species as analytes diluted in MQW. The HCl titrant was prepared from 37 mass % concentrated HCl (ACS grade), and the acid content of the titrant was determined prior to usage by titrating a carbonate standard solution (1000 ppm Inorganic Ventures). The titration procedure consists of continuous acid addition under agitation (600 rpm) until 20 mL of acid has been dispensed, or until a pH below 3 is reached, at a pace regulated by the apparatus based on the instantaneous temperature-corrected pH measurement. The start and end points are determined from the minimum of the derivative of the pH evolution as a function of the volume of acid dispensed.

**UV-Visible Spectrophotometry.** Chloride concentrations in solution was determined using the iron(III) thiocyanate method with an UV-visible spectrophotometer (Hach DR1900) and DPD testing kits (TNTplus-879). After zeroing using a blank reference, sample vials were measured in the ranges of 1–70 and 70–1000 mg/L.

**3.4. Gas Analysis. Gas Chromatography.** Gas chromatography (GC) was used to quantify CO<sub>2(g)</sub> evolution using an Inficon Micro GC Fusion instrument. The GC was calibrated using standard CO<sub>2</sub> calibration gases of 0, 0.1, 5, and 20 mol. % CO<sub>2</sub> with N<sub>2</sub> for balance. The apparatus allows for a carrier gas with a known and fixed flow rate that first passes through a hermetically closed reactor vessel where the reaction of interest occurs before/while being fed into the Inficon Micro GC instrument for analysis. The concentration of CO<sub>2</sub> in mol. % is recorded at intervals of 30 s for the entire reaction time and is then used to quantify the total amount of CO<sub>2</sub> emitted during the reaction by integration from the known flow rate of the carrier gas.

**3.5. Thermodynamic Modeling.** Thermodynamic modeling of solid- and solution-phase equilibria was carried out using GEM-Selektor v.3.6 (GEMS)<sup>76,77</sup> which incorporates the slop98.dat and Cemdata18 thermodynamic databases.<sup>62,78–80</sup> Property inputs from these databases are used to assess solid phase solubilities and aqueous speciation. To represent the non-ideality of the solutions, the activity coefficients were calculated using the Truesdell–Jones extension to the Debye–Hückel equation that is applicable for  $I_m \approx 2$  mol/L:<sup>81</sup>

$$\log \gamma_i = \frac{-A_\gamma z_i^2 \sqrt{I}}{1 + aB_\gamma \sqrt{I}} + b_\gamma I + \log \frac{X_{jw}}{X_w} \quad (2)$$

where  $\gamma_i$  is the activity coefficient and  $z_i$  is the charge of the  $i$ th aqueous species,  $A_\gamma$  and  $B_\gamma$  are the temperature- and pressure-dependent coefficients,  $X_{jw}$  is the molar quantity of water,  $X_w$  is the total molar amount of the aqueous phase, and  $I$  is the molal ionic strength. A common ion size parameter ( $a = 3.72$  Å) and a short-range interaction parameter ( $b_\gamma = 0.64$  kg/mol) were used, considering NaCl as the background electrolyte.<sup>81,82</sup>

**3.6. ZeroCAL Process. Ca Extraction and Complexation.** The solubility and dissolution rates of the AR calcite and limestone rock were investigated in EDTA-containing solutions of varying pH 6–10 and EDTA concentration 2–200 mmol/L. First, H<sub>4</sub>EDTA was fully dissolved in MQW in borosilicate beakers at room temperature under continuous agitation by the progressive addition of solid NaOH until the target pH was attained. Following the dissolution of EDTA, calcite or limestone was added so that the total calcium content in the system is slightly in excess vis-à-vis the EDTA amount, i.e., such that CaCO<sub>3</sub> (in mol) = 1.1 × EDTA (in mol). Considering solid-to-liquid ratios (s:l) on a g/g basis, where solid designates the calcium source and liquid designates the EDTA-containing solution, this corresponds to ratios of 1:4542, 1:454, and 1:45 for solutions containing 2, 20, and 200 mmol/L EDTA, respectively. The system was agitated at room temperature until it stabilized, that is, no further change in Ca concentration is observed. The time required to reach equilibrium, i.e., at least 95 mol. % Ca extraction, is dependent on pH and EDTA concentration as detailed in Table A2 (in the Appendix) but less than ~1.5 h in all cases. The solution and the headspace gas phase were both sampled and analyzed using ICP-OES, titration, and gas-phase (GC) analysis.

The evolution of the calcium concentration ([Ca], in mol/L) over time resulting from the dissolution of the calcium precursors can be modeled using a first-order equation of the form

$$[\text{Ca}] = \frac{k_0}{k_1} (1 - e^{-k_1 t}) \quad (3)$$

where  $k_0$  (in mol/L/s) and  $k_1$  (in s<sup>-1</sup>) are the apparent rate constants that are dependent on the pH and EDTA concentration and  $t$  is the time (s). The dissolution rate ( $r$ , in mol/m<sup>2</sup>/s) is calculated using the following equation:<sup>83</sup>

$$r = \frac{m_{\text{Ca}}}{\text{SSA}_t \times \Delta t \times m_{\text{CaCO}_3}} \quad (4)$$

where  $m_{Ca}$  is the amount of calcium (in mol) dissolved during the time  $\Delta t$  (s),  $m_{CaCo_3}$  is the initial mass of calcite introduced in the reactor (in g), and  $SSA_t$  is the specific surface area of the sample at a time  $t$  (in  $m^2/g$ ) calculated as follows:<sup>84</sup>

$$SSA_t = SSA(1 - FSD)^{2/3} \quad (5)$$

where  $SSA$  is the initial specific surface area calculated from the PSD of the sample and  $FSD$  is the fraction of solid dissolved (unitless) at any time  $t$  calculated as follows:

$$FSD = \frac{[Ca]_t}{\frac{n_{Ca}}{V}} \quad (6)$$

where  $[Ca]_t$  is the calcium concentration at a time  $t$ ,  $n_{Ca}$  is the amount of calcium initially available in the solid sample (in mol), and  $V$  is the volume of solution in the reactor (in L).

**Ca/CO<sub>2</sub> Separation and Na-HCO<sub>3</sub>/Water Separation via Nanofiltration.** A Sterlitech CF042 PTFE cross-flow cell<sup>85</sup> was used at a constant applied pressure of 80 psi (5.5 bar) provided by a diaphragm pump. The setup used a jacketed reactor connected to a chiller system for temperature control of the feed solution at 20 °C. The membranes were equilibrated by immersion for at least 24 h in the testing solution and stabilized/compacted under pressure for at least 1 h to achieve pseudo-steady state rejections and flux. The NF tests were carried out under batch-recirculation conditions, i.e., by circulating the retentate back to the feed tank under atmospheric pressure, at constant temperature and applied pressure<sup>86</sup> at selected water recoveries. The membranes were screened based on the reported normalized permeate flux and observed rejections (Table 2), and the experimental rejections and specific energy intensity as a function of water recovery for the solution system of interest herein (refer to Section A4 in the Appendix for the relevant equations). In the screening process for Ca-EDTA/Na-HCO<sub>3</sub> separations at 10–20 mmol/L in MQW, with and without high NaCl salinity background matrix, five membranes—N90, TS40, NF270, XN45, and NFW—were tested at a water recovery of 0% to limit concentration polarization effects recirculating both retentate and permeate streams, as well as at an increased water recovery of up to 50%, without recirculation of the permeate thereafter. This allowed examination of the separation and permeability properties to select a membrane for the high water recovery target of 85% (i.e., which yields the largest separation), typical of NF processes (80–90%).<sup>58,86,87</sup> The Na-HCO<sub>3</sub>/water separation for process-water recycling was performed at 75% water recovery upon screening of four membranes (NF90, TS80, SB90, and NP030).

**Ca Decomplexation and EDTA Recovery.** Acidification using electrolytically produced HCl is used to decomplex Ca from the EDTA, while ensuring its reprotonation into the highly insoluble H<sub>4</sub>EDTA form. Thus, HCl was used to titrate the Ca-EDTA solutions in MQW with EDTA contents ranging from 10 to 1000 mmol/L until HCl (in mol) = 4 × EDTA (in mol) has been introduced (i.e., when the EDTA is tetra-protonated). The precipitate was recovered by vacuum filtration using a Büchner apparatus and filter paper (Whatman, grade 1, >11 μm) and dried in a vacuum desiccator at room temperature prior to XRD and FT-IR analysis. The filtered solution was also analyzed so

that the residual contents of aqueous EDTA, and Ca and Cl could be quantified by titration, ICP-OES analysis, and UV–visible analysis, respectively.

**Ca(OH)<sub>2</sub> Precipitation.** Ca(OH)<sub>2</sub> precipitation was assessed using thermodynamic modeling and validated experimentally (Figure A8a in the Appendix) by titrating model “CaCl<sub>2</sub>/(1 - x)NaHCO<sub>3</sub>” solutions where 0.90 < x < 1.0 on a mole basis in MQW with 1 mol/L NaOH solutions. This range was selected to assess the precipitate purity in the range of Ca-EDTA/Na-HCO<sub>3</sub> separation achievable via NF in single and double stages (Step 2a-i). The recovered solids were dried under vacuum in glass desiccators to prevent carbonation prior to characterization.

The ZeroCAL process implies the use of recently developed flow electrolyzers to produce acidity (HCl) and basicity (NaOH). These bifurcated anode–cathode flow “seawater” electrolyzers were developed to enable atmospheric carbon dioxide removal and hydrogen production via the Equatic process (“Project SeaChange”).<sup>35,36</sup> These electrolyzers—which are fitted with OSA catalysts—have been upsized and field-demonstrated from the bench (0.001 kW) to pilot (10 kW) scale over the past several years. Based on operational data using a seawater feed, these electrolyzers currently achieve a Faradaic efficiency [the Faradaic efficiency (FE, unitless) is defined in terms of the known quantity of reagent stoichiometrically converted into desired product(s), as measured by the current passed. The overall system’s energy efficiency is defined as the product of the voltage efficiency and Faradaic efficiency] of >80% with respect to the production of OH<sup>-</sup> species at a cell voltage of ~-3 V, and hence Ca(OH)<sub>2</sub>, and a cell voltage that shows a change ( $\Delta V$ ) of <0.2 V over 7 days of continuous operations. Herein, the electrolyzer performance was based on the solubility of Ca(OH)<sub>2</sub> considering a seawater electrolyte of ~0.5 mol/L of NaCl and  $\sigma \approx 50$  mS/cm within the ZeroCAL process. First, the amount of OH<sup>-</sup> produced in the cathode half-cell was calculated as

$$[OH^-] = \frac{\alpha I}{FS} \quad (7)$$

where  $[OH^-]$  is the concentration of OH<sup>-</sup> ions in the catholyte (mol/L),  $\alpha$  is the current efficiency ratio or so-called “Faradaic efficiency”,  $I$  is the imposed current (A, for constant current operations),  $F$  is Faraday’s constant (96485 s·A/mol), and  $S$  is the electrolyte flow rate (L/s) through the electrolyzer. The  $[OH^-]$  concentration is sufficiently high such that, in general, pH > 12.5 is produced in the electrolyzer. Such high pHs are required to induce Ca(OH)<sub>2</sub> precipitation. For a Ca-enriched solution that transits the flow electrolyzer, the amount of Ca converted into Ca(OH)<sub>2</sub> can be estimated based on the difference in the inlet and outlet Ca concentrations, or the change in pH from the inlet to the outlet considering the valence (charge) mismatch between divalent calcium, and univalent hydroxyl species:

$$[Ca^{2+}]_{inlet} - \Delta[Ca^{2+}] = [Ca^{2+}]_{outlet} \quad (8)$$

$$2\Delta[OH^-] = \Delta[Ca^{2+}] \quad (9)$$

where  $\Delta[Ca^{2+}]$  and  $\Delta[OH^-]$  indicate the quantity of the Ca(OH)<sub>2</sub> precipitate (mol). By integrating eqs 7–9 and considering the  $K_{sp}$  of portlandite, it is found that  $\Delta[Ca^{2+}]$  is a function of the inlet Ca concentration ( $[Ca^{2+}]_{initial}$ ), the Faradaic efficiency, the dosage of OH<sup>-</sup> ions, and the solution



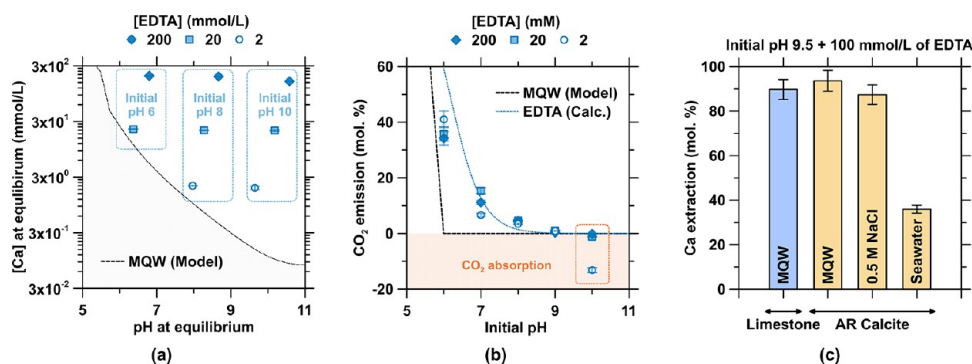


**Figure 3.** Dissolution of calcite at room temperature in the presence of EDTA. (a) Increased solubility of calcite (i.e., Ca concentration) as a function of the pH across a range of EDTA concentrations. The black dashed line shows the thermodynamically modeled solubility of calcite in a system devoid of EDTA. (b) Degassing of CO<sub>2</sub> expressed as a molar percentage of total amount of aqueous and mineralized carbonates in the system as a function of the EDTA concentration and the initial pH of the solution. The dashed black line shows the thermodynamically modeled CO<sub>2</sub> emission from calcite in a system devoid of EDTA, and the blue dotted line shows the CO<sub>2</sub> emission of calcite in a system containing EDTA calculated using eqs 12–14. (c) Ca concentration at equilibrium at pH 9.5 and in the presence of 100 mmol/L EDTA in MQW, a 0.5 mol/L NaCl solution, and simulated seawater (“Instant Ocean Seawater: IOSw”) for reagent calcite (AR calcite) or limestone rock.

(electrolyte) flow rate that establishes the residence time of Ca species within the electrolyzer (Section A1.2 in the Appendix for details):

$$\Delta[\text{Ca}^{2+}] = f\left(\frac{\alpha I}{S}, [\text{Ca}^{2+}]_{\text{inlet}}\right) \quad (10)$$

The electric energy intensity (EEI, MWh/t<sub>Ca(OH)<sub>2</sub></sub>) is determined from the ratio between the power input into the electrolyzer (i.e., the product of current input, and measured cell voltage) and the rate of Ca(OH)<sub>2</sub> precipitation as described below:

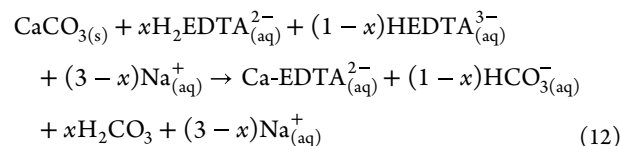
$$\text{EEI} = \frac{UI}{\Delta[\text{Ca}^{2+}] \times S \times M_{\text{Ca(OH)}_2}} \quad (11)$$

where  $M_{\text{Ca(OH)}_2}$  is the molar mass of portlandite and  $U$  (in V) is the measured voltage, wherein the thermodynamic minimum voltage,  $U_0 = -2.06$  V, is defined by the OER and HER half-cell reactions (eqs A1 and A2 in the Appendix).<sup>35,36</sup>

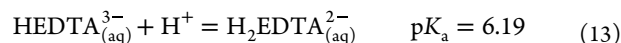
## 4. RESULTS AND DISCUSSION

**4.1. Ca Extraction (Dissolution) and Chelator Complexation.** In aqueous solution, EDTA binds cations with an increasing preference for valence and field strength— $Z/i_r$ , m<sup>-1</sup>, i.e., the ratio of the valence ( $Z$ ) to the ionic radius ( $i_r$ ). On account of its ability to bind divalent cations, EDTA substantially enhances the solubility of calcite (CaCO<sub>3</sub>; Figure 3a) by up to ~3 orders of magnitude compared to MQW. This occurs as EDTA chelates calcium species on a stoichiometric basis over a broad pH range: on average,  $0.96 \pm 0.04$  mol of Ca are bound per mol of EDTA at equilibrium. This ensures that EDTA is fully chelated, consistent with literature reports.<sup>33</sup> The reaction of EDTA with calcite evolves some CO<sub>2</sub> under specific conditions,  $6 < \text{pH} < 9$ , although no CO<sub>2</sub> evolution is observed when dissolving calcite in MQW (Figure 3b). This is because while the majority of the aqueous EDTA species are being held in the form of HEDTA<sup>3-</sup> anions above pH 6—as disclosed by the Bjerrum diagram (Figure

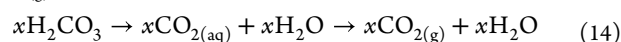
1b)—minor amounts of H<sub>2</sub>EDTA<sup>2-</sup> exist in solution so the dissolution reaction may be written as follows:



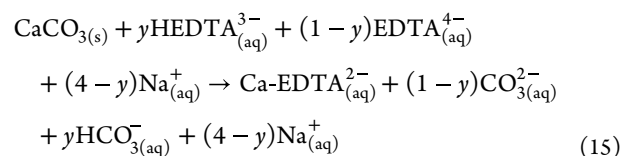
where  $0 < x < 1$  is dictated by the pK<sub>a</sub> of the following reaction:



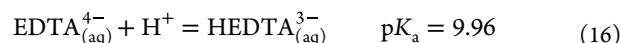
H<sub>2</sub>CO<sub>3</sub> eventually evolves as CO<sub>2(aq)</sub> and ultimately CO<sub>2(g)</sub>:



This reaction sequence is supported by the agreement between thermodynamic modeling (eqs 12–14) and experimental results (Figure 3b). Effectively, no CO<sub>2</sub> evolution is observed when calcite is dissolved in the presence of EDTA at an initial pH > 9, and net CO<sub>2</sub> absorption from ambient air is observed at yet higher pHs (Figure 3b). With increasing pH, the speciation of EDTA and DIC shifts toward their fully deprotonated forms (Figure 1b), and the dissolution reaction may be written as follows:



where  $0 < y < 1$  is dictated by the pK<sub>a</sub> of the following reaction:



At an initial pH of 9.5 and using 100 mmol/L EDTA—conditions at which no CO<sub>2</sub> evolution is expected—Ca extraction from limestone rock by EDTA is similar to that of AR-grade calcite (Figure 3c), despite small quantities of other solutes present in the rock. Since an electrochemical process requires a conductive electrolyte, dissolution was

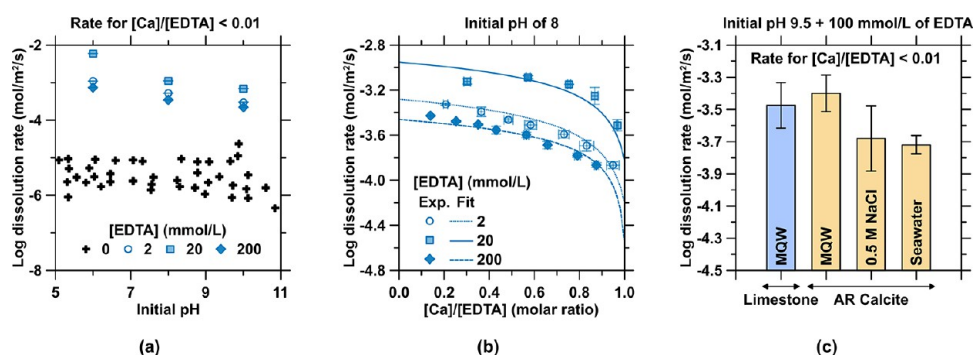


**Figure 4.** (a) “Initial” dissolution rate of calcite at high undersaturation (i.e., far from dissolution equilibrium) as a function of the initial pH of the solution across a range of EDTA concentrations. The data for dissolution occurring in MQW (“0 mmol/L EDTA”) are taken from the literature.<sup>24,89,90</sup> (b) Measured and fitted (eq 3) relationship between the dissolution rate and the  $[Ca]/[EDTA]$  (molar) ratio. (c) Dissolution rates of reagent-grade calcite and limestone rock at pH 9.5 and in the presence of 100 mmol/L EDTA in MQW, 0.5 mol/L NaCl, and simulated seawater (IOSw).

evaluated in a 0.5 mol/L NaCl solution and in synthetic Instant Ocean seawater to examine how salinity and ionic strength affects Ca-extraction behavior. It is noted that a “high” ionic strength alone does not affect the amount of extracted calcium in solution at equilibrium (Figure 3c). Rather, seawater is observed to strongly decrease the capacity of EDTA to extract calcium due to the native presence of  $\sim 55$  mmol/L Mg and  $\sim 10$  mmol/L Ca. These divalent “matrix cations”, particularly Mg, consume the chelation capacity of EDTA, and therefore compromise Ca chelation by EDTA, reducing its ability to uptake Ca species dissolved from calcite. This indicates that the use of natural brines and saline waters within the ZeroCAL process would require water softening, e.g., preprocessing by NF, to remove parasitic and competitive divalent cations such as Mg that may complex with EDTA.<sup>37,39,88</sup>

Considering the effects of EDTA on calcite dissolution, it is noted that EDTA enhances the dissolution rate of calcite enormously, as compared to MQW, across a range of pHs (Figure 4a).<sup>24,33</sup> In the presence of EDTA, increasing calcite dissolution rates are observed with decreasing pH (Figure 4a), at an EDTA dosage of  $\sim 20$  mmol/L EDTA (Figure 4a,b), and at low  $[Ca]/[EDTA]$  ratios (Figure 4b, where  $0 < [Ca]/[EDTA] < 1$ , molar ratio). The highest dissolution rates at  $[EDTA] \sim 20$  mmol/L arise from the competing effects of EDTA’s chelation properties (favorable) (Figure 4a) and increasing ionic strength (unfavorable) (Figure A3a in the Appendix) on the dissolution rate. The dissolution rates at saturation (i.e., where  $[Ca]/[EDTA] = 1$ ) imply that longer times would be required to reach saturation for 200 mmol/L EDTA solutions as compared to 2 or 20 mmol/L EDTA solutions, although the former solution contains 100 or 10 times as much extracted Ca as the latter solutions. Under similar pHs and EDTA concentrations, the AR calcite and the limestone rock feature similar dissolution rates (Figure 4c). The 0.5 mol/L NaCl solution and seawater perform similarly to each other and induce a decrease in the dissolution rate, whereby a linear decrease in the dissolution rate is observed with an increasing ionic strength (Figure A3a in the Appendix).

**4.2. Aqueous-Phase Separation of Ca-EDTA Complex and  $HCO_3^-$  Anions by NF.** The mildly alkaline leachate,  $9.5 < pH < 10.2$ , from the dissolution step that contains the Ca-EDTA complex and dissolved  $HCO_3^-$  anions and other species needs to be processed to separate

the Ca-rich and bicarbonate components, i.e., to allow for downstream  $Ca(OH)_2$  precipitation. This allows aqueous-phase stabilization of  $CO_2$  in the form of  $HCO_3^-$  at the prevailing pH in solution, avoiding the degassing/emission of  $CO_2$ . Dialytic NF using a negatively charged membrane enables separation of the Ca-EDTA complex and  $HCO_3^-$  anions via a combination of size and charge exclusion by retaining Ca-EDTA species in the “retentate” stream, while permeating  $Na^+ + HCO_3^-$  species in the “permeate” stream.<sup>51</sup> A suitable NF membrane ensures a high “Ca/ $CO_2$  separation”, i.e., high Ca-EDTA rejection and low monovalent rejection, as well as high flux, thereby reducing the required membrane area and operational energy at increasing water recovery. An initial screening of selected membranes at 0% water recovery (Figure 5a)—where concentration polarization effects are minimized—and a comparison of their performance relative to the XN45 membrane at increasing water recovery up to 50% (Figure 5b) reveals that, while Ca-EDTA rejection is 100% in all cases, the XN45 membrane is the most permeable to monovalent species ensuring the largest Ca/ $CO_2$  separation at a relatively high flux. Unsurprisingly, as the water recovery increases to 85%, the permeate flux drops as the concentration polarization magnifies (i.e., the ionic strength increases and the ratio of the applied pressure to osmotic pressure decreases in the feed stream; Figure A4a in the Appendix). The XN45 membrane remains effective enough for practical processing, e.g., featuring a flux of 1–7 L/(m<sup>2</sup>·h·bar). Importantly, the Ca-EDTA is fully rejected by the XN45 membrane, while  $Na^+ + HCO_3^-$  permeance increases with water recovery (Figure A4b in the Appendix). An apparent negative rejection is observed at  $>75\%$  water recovery (Figure A4c in the Appendix) due to the Donnan equilibrium that emerges at high concentration polarization at the surface of charged membranes.<sup>91–93</sup> As a result, at 85% water recovery, the concentration factor for Ca-EDTA is around  $7 \times$  compared to the feed stream, and the bulk Ca/ $CO_2$  separation, i.e.  $HCO_3^-$  permeation, is 85–90% at pH 8–10, for both limestone rock and AR-grade calcite streams—with and without a high salinity matrix (e.g., seawater; Figure 5c).

Improved separation is attainable: (i) for a single-stage system at slightly greater water recoveries due to the very steep increase in concentration factors and monovalent permeance at very high water recoveries (Figure A4a,b in the

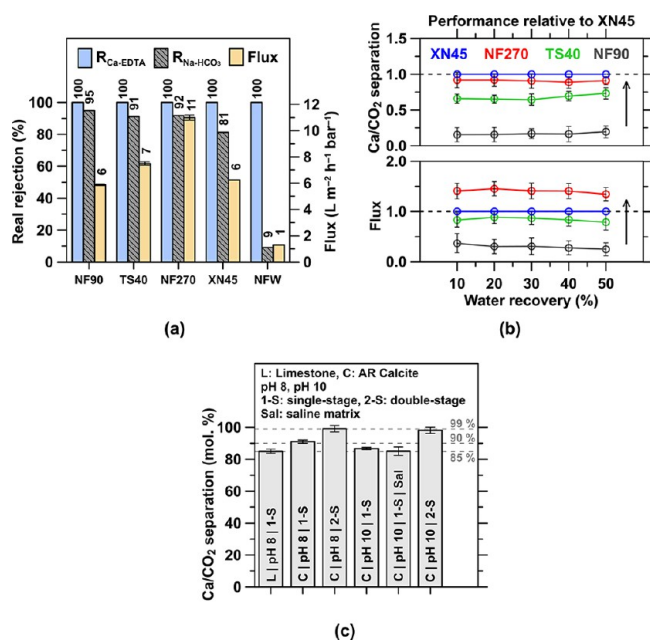


**Figure 5.** (a) Experimental performance of the selected NF membranes for Ca/CO<sub>2</sub> [Ca-EDTA and Na<sup>+</sup> + HCO<sub>3</sub><sup>-</sup>] separation at 0% water recovery. Here,  $R_{Ca-EDTA}$  and  $R_{Na-HCO_3}$  indicate the rejection of the Ca-EDTA<sup>2-</sup> and Na<sup>+</sup>-HCO<sub>3</sub><sup>-</sup> species, respectively. An optimal membrane maximizes  $R_{Ca-EDTA}$ , minimizes  $R_{Na-HCO_3}$ , and ensures a suitable flux at increasing water recovery. (b) Upon initial screening, Ca/CO<sub>2</sub> separation and flux of the remaining membrane candidates relative to the XN45 membrane up to 50% water recovery are shown, highlighting the Ca/CO<sub>2</sub> separation properties of XN45. (c) XN45 membrane's separation of Ca/CO<sub>2</sub> at 85% water recovery for limestone rock and AR-grade calcite precursors at pH 8 and 10, for single- and double-stage separation, using water and a high salinity simulated seawater matrix.

Appendix), albeit at the expense of an increasing energy demand, or (ii) by using a two-stage system that makes use of a rediluted Ca-EDTA-rich stream which enhances cumulative HCO<sub>3</sub><sup>-</sup> permeance to a level of ~99% (Figure 5c). In spite of the high water recovery, salt crystallization was not observed on the NF membranes given that the diffusing species (NaCl, NaHCO<sub>3</sub>, and NaOH) are highly soluble and the solution did not reach saturation. It is unsurprising that this approach is very effective at Ca-EDTA separations, given that prevailing EDTA concentrations are well below the chelant solubility: ~0.4 g<sub>EDTA</sub>/g<sub>water</sub> at 10 < pH < 11.<sup>94</sup> While the molecular size of Ca-EDTA (~3 × 10<sup>2</sup> Da) is on the order of the membrane pore size (~5 × 10<sup>2</sup> Da),<sup>69</sup> it is electrostatically repelled on account of its divalent negative net charge (Ca-EDTA<sup>2-</sup><sub>(aq)</sub>) by the membrane's surface whose functional groups are negatively charged in that pH range.<sup>95</sup> It should be noted that the observed difference in separation performance of the limestone rock and calcite feedstock is largely attributable to the aqueous phase contaminants introduced by the former, and from pH 8–10 due to carbonate speciation. Finally, it should be noted that the pH of the postseparation retentate and permeate remain similar, 9 < pH < 10, ensuring that dissolved carbonate species remain stable in their ionic HCO<sub>3</sub><sup>-</sup> form (Figure A4d in the Appendix). This is valid for both MQW (i.e., a solution containing stoichiometric amount of Ca-EDTA<sup>2-</sup>, HCO<sub>3</sub><sup>-</sup>, and Na<sup>+</sup>)

and in saline environments (i.e., a solution containing additional NaCl): the solution is charge- and mass-balanced regardless of the ionic strength prior to NF separation, resulting in little to no change in pH during NF.

**4.3. Water Recycling and Reuse: Implementing a Once-through or Recycle-Loop Process?** Two pathways are proposed to manage the NaHCO<sub>3</sub> enriched permeate stream. In the first configuration where no process water reuse, recovery, or recycling is required—e.g., when utilizing seawater—the stream can be discharged into the ocean; an effectively limitless storage reservoir for bicarbonate species.<sup>96</sup> Thermodynamic modeling—that is validated experimentally (Figure A5 in the Appendix)—indicates that as long as this discharge stream is sufficiently diluted, e.g., by the use of well-established diffuser solutions to a level greater than 30 times,<sup>97,98</sup> no CO<sub>2</sub> will degas (Figure A5a in the Appendix) nor will any secondary aragonite precipitation occur (Figure A5b,c in the Appendix). While the ZeroCAL process effluents and discharge strategy are being designed and engineered to mitigate any changes to the receiving aqueous environment, more work is needed to understand how, at very large (“gigatonne”) scale and over long periods, ocean carbon storage may evolve.<sup>99</sup> This is mainly to understand/mitigate any potential detrimental ecosystem effects that could manifest, if unaddressed, in hyperlocal environments.<sup>100</sup> In the second configuration where internal process water recycling is desired, implementing another NF step on the permeate output with an energy intensity of ~3 kWh/m<sup>3</sup>, depending on the water recovery, allows for the recirculation of 42–85% of the process water, resulting in a less water-intensive process while concentrating the carbonate stream. Here, NF is imposed on this saline stream, beyond the seawater matrix background, because it allows for higher water recovery with larger flux (3–5-fold)<sup>101</sup> at a lower energy cost than RO, which rejects all ions.<sup>102,103</sup> For example, such recycling of process water allows for the concentration of Na-HCO<sub>3</sub> (rejection >95% using NF90 membrane; Figure A6a in the Appendix), while the alkalinity of the retentate stream, 8.8 < pH < 9.1, ensures that no CO<sub>2</sub> evolution (Figure A6b in the Appendix) will occur (Step 2a-ii in Figure 2 for this process water recycling implementation). While other solutions such as RO systems and evaporation ponds could be beneficial, they imply increases in energy intensity, or land-use (surface) area, perhaps with the benefit of allowing the recovery of even high solubility salts (e.g., NaHCO<sub>3</sub> and NaCl) from the process.<sup>104</sup>

**4.4. Ca Decomplexation from EDTA and Enabling EDTA Recovery and Reuse.** The acidification of the Ca-EDTA-complex-containing retentate stream from pH 8–10 down to pH < 2 utilizes 4 moles of HCl per molar unit of the Ca-EDTA complex (Step 2b), i.e., thereby utilizing 80 mol. % of the HCl produced alongside a stoichiometric quantity of NaOH. This acidification ensures the decomplexation of Ca from the EDTA while resulting in the precipitation of H<sub>4</sub>EDTA. Under acidic conditions, where typical Ca-bearing phases are unstable, Ca persists at high concentrations as a cationic species (Ca<sup>2+</sup>) in aqueous solution. The liberation of Ca from the Ca-EDTA complex occurs in the pH range of 3–4, as attested by the main peak shift and secondary peaks attenuation in the FT-IR spectra, while the precipitation of H<sub>4</sub>EDTA occurs at pH < 2.5 where the peaks of its aqueous forms diminish (Figure 6a). In addition, settling tests have shown that the reprecipitated

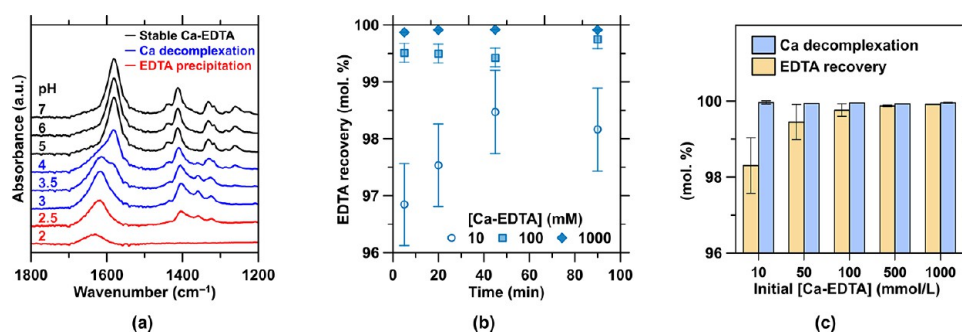


**Figure 6.** (a) FT-IR spectra of the Ca-EDTA complex for pHs ranging from 2 to 7 representing the regions of stability (complexation) and instability (decomplexation). (b) EDTA recovery efficiency as a function of the initial Ca-EDTA concentrations and time of acid exposure. (c) Ca decomplexation and EDTA recovery efficiencies for different Ca-EDTA concentrations after 90 min. In general, for EDTA concentrations >100 mmol/L, near stoichiometric recovery of the EDTA is observed within 5 min.

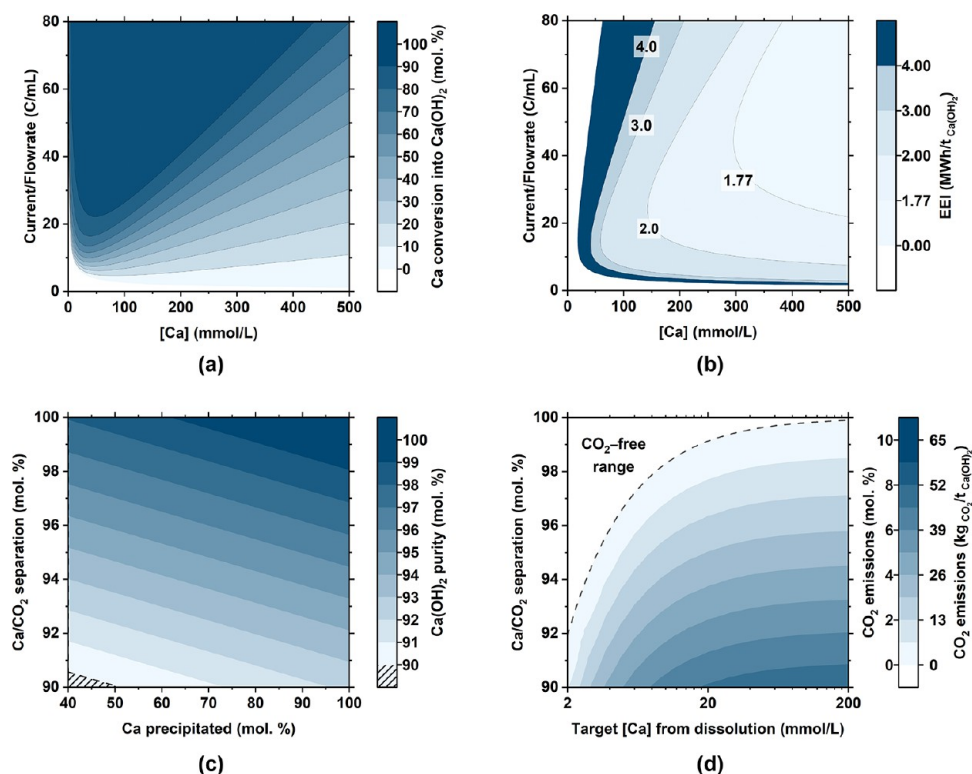


**Figure 7.** Electrolyzer performance for a Faradaic efficiency of 90% and a cell voltage of  $-2.06$  V showing (a) Ca conversion (into  $\text{Ca}(\text{OH})_2$ ) and (b) the electric energy intensity (EEI) of  $\text{Ca}(\text{OH})_2$  precipitation. Both parts a and b refer to  $\text{Ca}(\text{OH})_2$  precipitation (Step 3) only and are shown as a function of the inlet Ca concentration and the current/flow rate ratio. (c) Purity of portlandite produced as a function of the Ca/ $\text{CO}_2$  separation in solution after Step 2a-i. (d) Extent of  $\text{CO}_2$  degassing (as a percent of the amount of  $\text{CO}_2$  introduced into the system via the dissolution of limestone) that could occur as a function of the initial EDTA concentration and extent of Ca/ $\text{CO}_2$  separation after Step 2a-i.

EDTA settles quickly, with bulk settling occurring in a static system in a few minutes, indicating that recovery of the reprecipitated EDTA solids can be achieved using conventional clarifiers. The Ca decomplexation and EDTA precipitation process occurs rapidly, i.e., within 5 min (Figure 6b). While Ca is stoichiometrically liberated,  $\sim 100$  mol. %, recovery of EDTA progressively increases up to 99.9 mol. % with its increasing initial concentration (Figure 6c), i.e., as the intrinsic solubility limit of EDTA at pH 2 ( $\sim 0.1$  mmol/L) is achieved. Careful characterization of the  $\text{H}_4\text{EDTA}$  precipitate using FT-IR and XRD indicates that this product is analogous to the pristine AR-grade compound (Figure A7a in the Appendix), while Ca and Na salts

intrinsic to the system constitute an additional  $<1$  mol. % of the product. Importantly, the use of the reprecipitated material results in a  $\text{CaCO}_3$  dissolution behavior similar to its reagent-grade form (Figure A3b in the Appendix) over at least 5 cycles of Ca recovery and release, although the long-term cyclic performance remains to be established. It should be noted that while the recovery of EDTA is carried out using the acidity produced electrolytically, this acidification dilutes the Ca content of the solution as a function of the anolyte's acidity ( $\text{pH} \leq 1$ ) and the EDTA concentration after NF. Therefore, a terminal NF step (Step 2a-iii in Figure 2) is used to ensure a Ca-enriched solution for electrolytic precipitation. Neutralization of the  $\sim 20$  mol. %

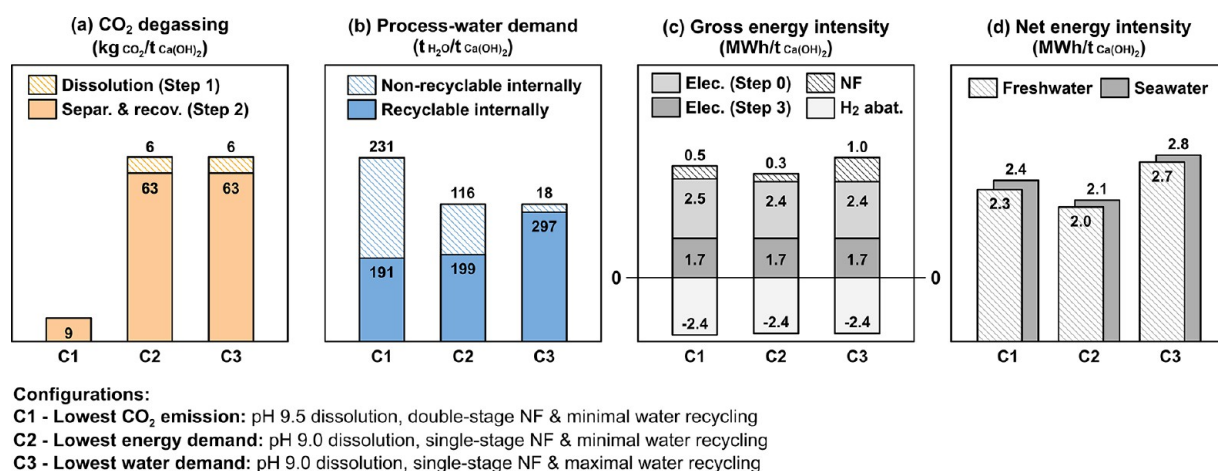


**Figure 8.** (a) CO<sub>2</sub> evolved (process emissions) across different configurations. (b) Process water demand, (c) gross energy intensity, and (d) net energy intensity of the ZeroCAL process considering Steps 0–3 across three different configurations (C1, C2, and C3) that encompass single- or double-stage NF (i.e., to minimize CO<sub>2</sub> evolution), with or without process water recycling (i.e., to reduce the water demand and/or the non-electrolysis process energy) for an initial Ca-EDTA concentration of 100 mmol/L. Herein, in part c, electrolytic Ca(OH)<sub>2</sub> precipitation (Step 3) is estimated to have a gross energy intensity of ~1.7 MWh/t<sub>Ca(OH)<sub>2</sub></sub>, while the remainder of the energy is attributed to “upstream” operations (Steps 0–2).

surplus HCl can be achieved via the dissolution of abundant and high H<sup>+</sup> neutralization capacity Ca/Mg-silicates, e.g., olivine (Mg<sup>2+</sup>, Fe<sup>2+</sup>)<sub>2</sub>SiO<sub>4</sub>.<sup>35</sup>

**4.5. Electrolytic Precipitation of Portlandite (Ca(OH)<sub>2</sub>) in Flow Electrolyzers.** The electrolytic precipitation of portlandite is readily induced by the alkalization of the Ca-enriched solution that is produced in Steps 2b/2a-iii using flow electrolyzers that have already been operated at the 10 kW pilot scale. In general, the performance of this electrolyzer configuration is described by the “current-to-flow rate” ratio [*I/S*; eqs 7–11], which describes the amount of current input that is needed to induce stoichiometric precipitation, i.e., 100 mol. % conversion of aqueous Ca into Ca(OH)<sub>2</sub>. The resulting energy intensity (Figure 7) drives reactions in the cathode half-cell where split water molecules produce OH<sup>−</sup> ions and thus a pH increase that promotes Ca(OH)<sub>2</sub> formation.

The calculated efficiency of Ca conversion into Ca(OH)<sub>2</sub> at varied inlet Ca concentrations and current/flow rate ratio and the corresponding EEI for precipitation only—i.e., Step 3 only, not including Steps 0–2—are shown in Figure 7a,b (eq 10 and Section A1.2 in the Appendix). In general, it is noted that, for inlet Ca concentrations ranging between 100 mmol/L < [Ca]<sub>inlet</sub> < 500 mmol/L and 20 C/mL < [*I/S*] < 40 C/mL, there exists an operational optimum wherein Ca(OH)<sub>2</sub> can be produced at an electrolyzer energy intensity of <2 MWh/t<sub>Ca(OH)<sub>2</sub></sub> (Figure 7a,b). This gross energy intensity for electrolytic portlandite precipitation implies a net energy intensity of <1 MWh/t<sub>Ca(OH)<sub>2</sub></sub> considering the energy embodied in the coproduced hydrogen (~39.4 MWh/t<sub>H<sub>2</sub></sub>)<sup>105</sup> and an energy conversion efficiency on the order of 80–90% via a combined heat and power fuel cell.<sup>106</sup>

An important aspect to consider in this system is the tendency to produce CaCO<sub>3</sub>, i.e., if any dissolved CO<sub>2</sub> in the form of HCO<sub>3</sub><sup>−</sup>/CO<sub>3</sub><sup>2−</sup> were to persist in the system, given the tendency of CaCO<sub>3</sub> to form at lower pHs than Ca(OH)<sub>2</sub> and, in turn, consume Ca in the system. This emphasizes the need to effectively remove dissolved carbonate via NF, failing

which (i) CaCO<sub>3</sub> impurities could be increasingly intermixed into the Ca(OH)<sub>2</sub> formed and/or (ii) CO<sub>2</sub> could degas during the acidic decomplexation and recovery of EDTA. Based on the thermodynamic modeling and experimental data (Figure A8a in the Appendix), it is clarified that achieving a Ca/CO<sub>2</sub> separation of >90 mol. % allows for high-grade Ca(OH)<sub>2</sub> production (Figure 7c) and minimizes the risk of CO<sub>2</sub> evolution during EDTA recovery (Figure 7d). Of course, minimizing CO<sub>2</sub> evolution implies minimizing the amount of carbonate in solution (Figure A7b in the Appendix). This suggests the use of a two-stage NF sequence and, likely, the provision of a seawater feed. It is additionally noted that the use of seawater, or natural limestone, is likely to introduce other impurities including silica, alumina, magnesia, ferrous-species, etc. Broadly speaking, most of these impurities exist at concentrations substantially lower than carbonate, and thus are disregarded at a first approximation. These contaminants may be removed using a pH swing in a judiciously selected pH range of ~11.0–11.5 (Figure A8b in the Appendix) that allows one to precipitate and separate a range of hydroxide species (e.g., Fe(OH)<sub>2</sub>, Fe(OH)<sub>3</sub>, Al(OH)<sub>3</sub>, and Mg(OH)<sub>2</sub>) as well as amorphous silica (SiO<sub>2</sub>) and a silicate hydrate phase that contains a small amount of magnesium and calcium (C-M-S-H)—at pHs inferior to Ca(OH)<sub>2</sub>—to thus produce high-purity portlandite.

## 5. PROCESS OUTLOOK AND GENERAL IMPLICATIONS

In general, considerations of Ca extraction (from limestone), its aqueous separation from “CO<sub>2</sub>” while preventing CO<sub>2</sub> degassing, and the electrolytic precipitation of Ca(OH)<sub>2</sub>, all appear reasonable (Figure 8 and Table A3 in the Appendix). Analysis of the consumable reaction stoichiometries (Section 2) shows that the production of 1 t of Ca(OH)<sub>2</sub> requires 1.35 t of CaCO<sub>3</sub>, 1.09 t of water, and 0.79 t of NaCl. It should be noted that ~75 mol. % of the NaCl used as electrolyte is recycled during the process (Section 2: Steps 2a and 2b). In addition, ~100 mol. % of the EDTA used is

recovered and reused allowing use of a pH-swing cycle that minimizes additive demand. Aside from the (sea)water consumed, i.e.  $\sim 1 \text{ t}_{\text{H}_2\text{O}}/\text{t}_{\text{Ca}(\text{OH})_2}$ , the process water demand depends on (i) the initial EDTA concentration and (ii) the amount of water that is recycled internally (Step 2a-ii) [N.B.: without the use of a chelator, the water demand would increase  $\sim 100$  times]. The process coproduces 68 kg of  $\text{H}_2$ , 0.54 t of  $\text{O}_2$ , 0.49 t of HCl, and 1.13 t of  $\text{NaHCO}_3$  per t of  $\text{Ca}(\text{OH})_2$ . The  $\text{H}_2$  coproduct from the Step 0 and Step 3 electrolysis can be co-combusted with oxygen to heat the cement kiln or produce electricity,<sup>105,106</sup> abating/offsetting  $\sim 2.4 \text{ MWh}/\text{t}_{\text{Ca}(\text{OH})_2}$  of the energy demand. This reduces the gross energy intensity, across all steps (Steps 0–3), resulting in a net energy intensity ranging between 2.0–2.8  $\text{MWh}/\text{t}_{\text{Ca}(\text{OH})_2}$  for different process configurations (Figure 8b,c). The HCl coproduct 0.1–0.3 mol/L is used internally for EDTA recovery and pH conditioning within the process (80 mol. %), whereas the surplus (20 mol. %) can be either concentrated and sold or neutralized using geological rock feedstocks prior to discharge.<sup>35</sup> Two management options for the carbonate stream (0.1 mol/L of  $\text{NaHCO}_3$ ) are proposed: (i) discharge into the ocean or riverine discharge to ensure carbon storage under conditions of infinite dilution (La Plante et al.)<sup>35,36</sup> reserved ecosystemic considerations to be established at scale or (ii) concentration up to  $\sim 0.7 \text{ mol/L}$   $\text{NaHCO}_3$  to enable the recovery of “dilute soda” for utilization.<sup>107</sup> Of note, the NF separations implied by this process on account of strong Ca binding (by the chelator) are not susceptible to mineral scaling. However, if it does occur, a simple pH-swing for cleaning (e.g., using the surplus acid) has been shown to restore membrane performance, a standard operating process in desalination plants.<sup>107</sup>

Further analysis of  $\text{CO}_2$  evolution during the process indicates a vanishingly small  $\text{CO}_2$ -intensity—i.e., process emissions as low as 1.5 mol. % of the total mineralized  $\text{CO}_2$  contained in the limestone, equivalent to  $\sim 9 \text{ kg}_{\text{CO}_2}/\text{t}_{\text{Ca}(\text{OH})_2}$ ; see Configuration C1—as long as dissolution is carried out at slightly alkaline pH (9.5) and two-stage NF is used to ensure superior Ca/ $\text{CO}_2$  separation (Figure 8a). This configuration, however, implies a substantial process water and energy demand (Figure 8). Configuration C2 offers significant reductions of the energy demand by only using a single-stage NF system and minimal process water recycling (Figure 8d). Reducing the amount of process water recycling lowers the energy demand, a configuration of interest if seawater or saline groundwater is used as the electrolyte in near-coastal regions. In water-stressed areas, Configuration C3 offers the lowest process water demand by maximizing the amount of internal recycling (NF step 2a-ii) while increasing the energy demand and the amount of  $\text{CO}_2$  evolved in the process.

Taken together, the ZeroCAL process ultimately offers  $>98\%$  process- $\text{CO}_2$  emissions reductions while requiring  $\sim 2$  times the total energy demand of conventional lime manufacturing, or limestone decarbonization, i.e. typically within 1.0–1.4 MWh per t of PC (clinker),<sup>8–11</sup> quicklime ( $\text{CaO}$ ), or portlandite ( $\text{Ca}(\text{OH})_2$ ) production.<sup>4–7</sup> This energy demand, however, is determined based on the simple linear additivity of process unit operations. Although much work remains to integrate this multistep process, across unit operations effectively, preliminary process intensification (PI) studies indicate that the energy demand of the ZeroCAL

process can be reduced by  $\sim 30\%$  across all noted configurations, resulting in near-parity with existing thermochemical methods for limestone’s decarbonation during PC production. As one example, at atmospheric pressure,  $\text{Ca}(\text{OH})_2$  decomposes into  $\text{CaO}$  at a temperature that is  $\sim 250 \text{ }^\circ\text{C}$  lower than limestone. This allows for decarbonation processing to be completed in the preheater/precalciner such that the feed entering the kiln is ready for clinkering.

While there is a substantial demand for a finite albeit fast-growing supply of renewable energy, electrification allows a means for decarbonizing cement production while using  $\text{Ca}(\text{OH})_2$  as a zero-carbon emissions feedstock for existing cement plants, using adjacent limestone quarries, to produce PC—all without resorting to geological sequestration and its associated requirements of infrastructure, e.g., reservoirs, pipelines, compression stations, etc. That said, the ZeroCAL process does require substantial process water, which for near-coastal plants can be sourced from the ocean. Conveniently, multiple high-capacity cement plants are spatially distributed near coastlines and inland saline water sources, for instance, in the United States and Europe.<sup>15,23</sup> But, even plants distant from the coast often have access to substantial supplies of water, e.g., in the form of millions of cubic meters of “mine water” that rises from the water table over the course of quarrying operations and that is typically discharged as a waste. Such mine water is typically not saline, and would require NaCl dosing to be utilized within the paradigm of the ZeroCAL process to ensure valence compensation of discharged bicarbonate: 1  $\text{Na}^+$  cation per discharged  $\text{HCO}_3^-$  anion. Of course, in such circumstances, it would be important to consider and design the process discharge in such a way that it does not affect the salinity of prevalent groundwater in the discharge vicinity, or to reuse the discharged water during subsequent production cycles.

Heat and power account for  $\sim 30\%$  of the cost of PC production,<sup>108</sup> and  $\sim 90\%$  and  $10\%$  of the energy requirements,<sup>10,13</sup> respectively. Their cost basis, however, is subject to change as renewable generation expands making renewable electricity cheap,<sup>109</sup> and fossil fuels eventually become supply constrained and expensive.<sup>15,110,111</sup> Additionally, PC decarbonization can benefit from grants, tax credit, and Buy Clean opportunities,<sup>15</sup> which will make adoption more attractive. This is important since industrial decarbonization in the manner of the ZeroCAL process paves the way for<sup>112–114</sup> (i) a  $\text{CO}_2$ -free supply chain for traditional PC and lime production and (ii) opportunities to produce cementation agents based on  $\text{CO}_2$  mineralization with an energy intensity comparable to PC manufacturing but with a  $>90\%$  reduction in  $\text{CO}_2$  intensity.<sup>13,115–117</sup> Importantly, the ZeroCAL approach also opens up new pathways for (i) brucite ( $\text{Mg}(\text{OH})_2$ ) production from abundant basaltic and magnesite rocks at an even lower energy intensity than  $\text{Ca}(\text{OH})_2$  production due to the more favorable thermodynamics of precipitation<sup>118</sup> and (ii) carbon dioxide removal (CDR) using electrolytically produced, ultra-low carbon intensity portlandite and brucite precursors.<sup>117</sup> Significantly, this latter concept also enables steel decarbonization by providing  $\text{Mg}(\text{OH})_2$  or  $\text{Ca}(\text{OH})_2$  as a slag-forming  $\text{CO}_2$ -free feedstock (in lieu of limestone) for blast furnace operations, while hydrogen can be used not only to power a blast furnace, but also as a reducing agent in the direct reduction of iron (DRI) process. More broadly, but at smaller scales, a

zero-carbon lime is desirable for use in the energy industry,<sup>119–122</sup> soil and water,<sup>122</sup> food,<sup>123</sup> pharmaceutical,<sup>124,125</sup> and cosmetic<sup>126</sup> sectors. Further advancement of the ZeroCAL process encompasses activities including (i) electrolysis efficiency enhancement via cell design and electrode development and (ii) the use of better/alternative chelators with a smaller gap between the  $pK_a$  of the pristine and complexed species to reduce the intensity of the pH-swing (i.e., to reduce acid–base demands), while facilitating Ca/CO<sub>2</sub> separation and chelator recycling. Why does all this matter? Because based on current estimates, when powered by renewable energy, the ZeroCAL process can achieve >99% process CO<sub>2</sub> emissions reductions for a net energy intensity of <2 MWh/t<sub>Ca(OH)<sub>2</sub></sub>, thus unlocking a near-NPV parity pathway for decarbonizing PC, concrete, and steel production globally.<sup>127–129</sup>

## 6. SUMMARY AND CONCLUSIONS

The ZeroCAL process demonstrated herein establishes a near process-emissions-free pathway for decarbonizing portlandite and PC production, using limestone as a feedstock. *In situ* electrolytic acid/base generation enables a self-contained pH-swing process wherein EDTA-promotes CaCO<sub>3</sub> dissolution, while preventing CO<sub>2</sub> exsolution. Subsequent NF steps allow (i) effective Ca/CO<sub>2</sub> separation, (ii) process water recycling, and (iii) scalable discharge of CO<sub>2</sub> in the form of aqueous HCO<sub>3</sub><sup>−</sup> at sufficient alkalinity such that CO<sub>2</sub> can be stored durably and permanently in the near-surface environment. The effective (~100%) and cyclic use (complexation) and recovery (decomplexation) of EDTA and Ca/EDTA separation are demonstrated ensuring that, under relevant configurations, (sea)water, electricity, and limestone (and NaCl) form the only inputs of the process. Electrolysis of a Ca-enriched feedstream reveals that, at an optimal current/flow rate ratio, the net energy intensity of process for high-purity Ca(OH)<sub>2</sub> production at the current point in time, ~2 MWh per t of Ca(OH)<sub>2</sub>, is approaching similarity to conventional cement (PC) production. Importantly, electrification and hydrogen-based kiln heating of cement production create a new pathway for cement decarbonization that does not rely on geological sequestration—potentially simplifying PC decarbonization while mitigating the trajectory of ongoing and accelerating climate change.

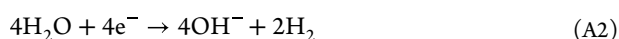
## APPENDIX

The Appendix includes additional data and details relevant to electrolysis, process stoichiometry, EDTA and CaCO<sub>3</sub> dissolution, membrane screening and performance, process water recycling and ocean carbon storage, EDTA recovery, Ca(OH)<sub>2</sub> electrolytic precipitation, and configuration-specific process conditions and carbon, water, and energy intensities.

### A1. ELECTROLYZER DEFINITION

#### A1.1. Step 0: Acid and Base Generation via Water Splitting.

Electrolytic water splitting in the flow electrolyzer considered herein follows the half-cell anodic (eq 1) and cathodic (eq 2) reactions:



The conductivity of the solution is a function of the presence of NaCl (~0.5 mol/L; similar to seawater), which theoretically allows Na<sup>+</sup> and/or Cl<sup>−</sup> to act as charge

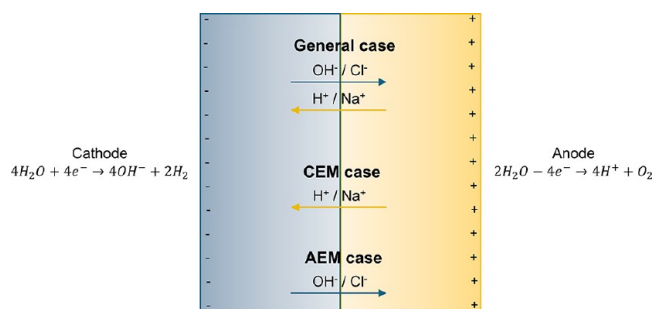
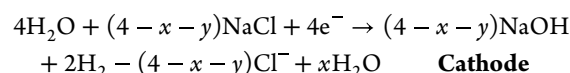
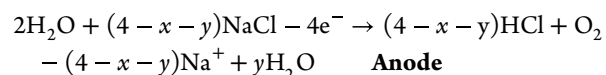


**Figure A1.** Schematic representation of the reactions and species migrations occurring in the electrolyzer. Species migrations are specified for the different types of membranes/separators that may be used to separate the anolyte and the catholyte, e.g., porous membrane (non-ion specific), cation exchange membrane (CEM), and anion exchange membrane (AEM).

compensators of the half-cell reactions by migration through the membrane separating the catholyte and the anolyte. Practically, the electroneutrality of both the catholyte and the anolyte is ensured by migration and diffusion of electroactive ions. Hence, solution-phase electroneutrality is assured by Na<sup>+</sup> and H<sup>+</sup> transfer from the anolyte to the catholyte and by Cl<sup>−</sup> and OH<sup>−</sup> from the catholyte to the anolyte.

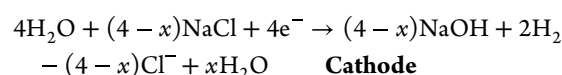
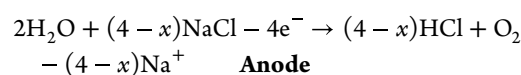
The most general case considers the use of a porous membrane (i.e., a non-ion-selective membrane) to separate the anolyte and the catholyte. In this case,  $x$  is the number of moles of H<sup>+</sup> crossing the membrane from the anolyte to the catholyte and  $y$  is the number of moles of OH<sup>−</sup> crossing the membrane from the catholyte to the anolyte. The reactions happening in the anolyte and the catholyte, considering the species migrations (i.e., the charge carriers) can be described as follows:

**Case 1:** General cases (non-ion-selective membrane)

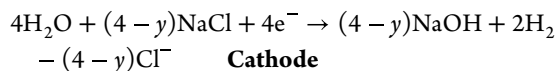
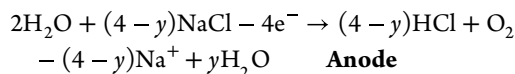


In most commercial cases, electrolyzers use ion-selective membranes (i.e., cation exchange membranes or anion exchange membranes). In those cases, the reactions are simplified, as only one type of ion can pass through the membrane:

**Case 2:** Cation exchange membrane (CEM,  $y = 0$ )

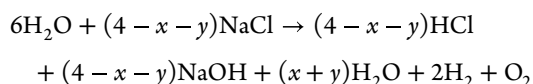


**Case 3:** Anion exchange membrane (AEM,  $x = 0$ )



Whether using one type of membrane or another depends on their efficiency for the process, as well as the electrical energy intensity reductions they allow. In the context of this study, electrolysis is considered for the general case (Case 1) which has been demonstrated at the pilot-scale. The overall reaction in the electrolyzer can be written as follows considering the two half reactions described above:

**Case 1:** General cases (non-ion-selective membrane)



### Overall reaction

The overall reaction depends on the ratio between  $\text{H}^+$ / $\text{Na}^+$  and  $\text{OH}^-/\text{Cl}^-$  migration through the membrane. A simplification can be made based on the following two hypotheses:

(1) The Peclet number in both cells favors migration by advection rather than diffusion.

(2) The Reynolds number is low enough so the solution inside one chamber cannot be homogenized by turbulence.

If those two conditions are met, which could be possible if the spacing between the electrodes is high enough and the flow rate low enough, then the  $\text{H}^+$  and  $\text{OH}^-$  produced at the electrodes should not be able to diffuse fast enough toward the membrane to be the charge carriers for the electroneutrality. In this case, only  $\text{Na}^+$  and  $\text{Cl}^-$  migration should be able to satisfy the solution electroneutrality. At greater pH gradients, the water-splitting ions can conduct more current via migration, and macroscopic charge neutrality can still be satisfied by counter-diffusion of the electrolyte ions through the diffusion layers. In both cases, the overall reaction may be simplified down to



### A1.2. Step 3: $\text{Ca}(\text{OH})_2$ Precipitation.

The addition rate of  $\text{OH}^-$  (in mol/L) in the flow electrolyzer catholyte can be calculated as described by eq 7. When portlandite precipitation attains equilibrium, the activities of the hydroxide and calcium ions in the effluent should ensure oversaturated conditions, i.e., the  $\text{OH}^-$  and the  $\text{Ca}^{2+}$  activity can be calculated by considering the  $K_{\text{sp}}$  of portlandite, such that

$$K_{\text{sp}} = \{\text{Ca}^{2+}\}\{\text{OH}^-\}^2 \quad (\text{A4})$$

where the  $\{\}$  indicate ion activities and  $K_{\text{sp}} = 5.2 \times 10^{-6}$  at  $p = 1$  bar and  $T = 25$  °C and

$$\{\text{CaOH}^+\} = k_{\text{CaOH}^+}\{\text{Ca}^{2+}\}\{\text{OH}^-\} \quad (\text{A5})$$

where  $k_{\text{CaOH}^+}$  is the equilibrium constant of the aqueous species  $\text{CaOH}^+$ . From the boundary conditions shown in Figure A2:

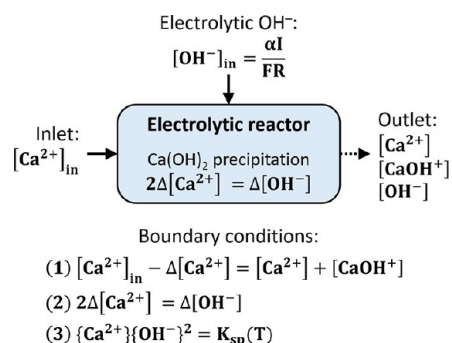


**Figure A2.** Schematic representation of the chemical boundary conditions considered in the flow electrolyzer.

$$\begin{aligned} [\text{Ca}^{2+}]_{\text{in}} - \Delta[\text{Ca}^{2+}] &= [\text{Ca}^{2+}] + [\text{CaOH}^+] \\ &= \frac{\{\text{Ca}^{2+}\}}{\gamma_{\text{Ca}^{2+}}} + \frac{\{\text{CaOH}^+\}}{\gamma_{\text{CaOH}^+}} \\ &= \frac{\{\text{Ca}^{2+}\}}{\gamma_{\text{Ca}^{2+}}} + \frac{k_{\text{CaOH}^+}\{\text{Ca}^{2+}\}\{\text{OH}^-\}}{\gamma_{\text{CaOH}^+}} \\ &= \{\text{Ca}^{2+}\} \left( \frac{1}{\gamma_{\text{Ca}^{2+}}} + \frac{k_{\text{CaOH}^+}\{\text{OH}^-\}}{\gamma_{\text{CaOH}^+}} \right) \\ &= \{\text{Ca}^{2+}\} \left( \frac{\gamma_{\text{CaOH}^+} + \gamma_{\text{Ca}^{2+}}k_{\text{CaOH}^+}\{\text{OH}^-\}}{\gamma_{\text{Ca}^{2+}}\gamma_{\text{CaOH}^+}} \right) \end{aligned} \quad (\text{A6})$$

where  $[\ ]$  indicates ion concentrations and  $\gamma$  indicates ion activity coefficients that can be calculated considering eq 2, such that

$$\{\text{Ca}^{2+}\} = \frac{\gamma_{\text{Ca}^{2+}}\gamma_{\text{CaOH}^+}([\text{Ca}^{2+}]_{\text{in}} - \Delta[\text{Ca}^{2+}])}{\gamma_{\text{CaOH}^+} + \gamma_{\text{Ca}^{2+}}k_{\text{CaOH}^+}\{\text{OH}^-\}} \quad (\text{A7})$$

and

$$\begin{aligned} \{\text{OH}^-\} &= \gamma_{\text{OH}^-}[\text{OH}^-] = \gamma_{\text{OH}^-}([\text{OH}^-]_{\text{in}} - 2\Delta[\text{Ca}^{2+}]) \\ &= \gamma_{\text{OH}^-} \left( \frac{\alpha I}{FS} - 2\Delta[\text{Ca}^{2+}] \right) \end{aligned} \quad (\text{A8})$$

where  $\alpha$  is the current efficiency ratio (0.9, unitless),  $I$  is the current (A, for constant current operations),  $F$  is Faraday's constant (96485 s·A/mol), and  $S$  is the solution flow rate (L/s) through the electrolyzer. Substituting eqs A7 and A8 into eq A4:

$$\begin{aligned} K_{\text{sp}} &= \frac{\gamma_{\text{Ca}^{2+}}\gamma_{\text{CaOH}^+}([\text{Ca}^{2+}]_{\text{in}} - \Delta[\text{Ca}^{2+}])}{\gamma_{\text{CaOH}^+} + \gamma_{\text{Ca}^{2+}}k_{\text{CaOH}^+}\gamma_{\text{OH}^-} \left( \frac{\alpha I}{FS} - 2\Delta[\text{Ca}^{2+}] \right)} \gamma_{\text{OH}^-}^2 \\ &\quad \times \left( \frac{\alpha I}{FS} - 2\Delta[\text{Ca}^{2+}] \right)^2 \end{aligned} \quad (\text{A9})$$

and by solving eq A9, eqs 10 and 11 are obtained.



## A2. PROCESS STOICHIOMETRY

Table A1. Experimental Verification of Stoichiometries and Mass and Charge Balances

process step	stoichiometric ratio (mol/mol)	mass balance (mol.)	charge balance
0 (anode)	$H^+/e^- = 0.9^a$		
0 (cathode)	$e^-/OH^- = 0.9^a$		
1a	NaOH/H <sub>4</sub> EDTA = 3.03 <sub>model</sub> / 2.78 <sub>exp.</sub> ± 0.04 (pH 8.5) NaOH/H <sub>4</sub> EDTA = 3.08 <sub>model</sub> / 2.89 <sub>exp.</sub> ± 0.03 (pH 9.0) NaOH/H <sub>4</sub> EDTA = 3.21 <sub>model</sub> / 3.07 <sub>exp.</sub> ± 0.04 (pH 9.5)		
1b	CaCO <sub>3</sub> /HEDTA <sup>3-</sup> = 1.0 ± 0.0		
2a-i		1.1 ± 0.1	1.0 ± 0.1 <sup>b</sup>
2a-ii		1.0 ± 0.1	1.1 ± 0.1 <sup>b</sup>
2b-i	HCl/Ca-EDTA = 4.0 with final pH 1.82 <sub>model</sub> /1.87 <sub>exp.</sub> ± 0.09		
3	NaOH/Ca(OH) <sub>2</sub> = 2.0 <sub>model</sub> / 2.2 <sub>exp.</sub> ± 0.3		

<sup>a</sup>Faradaic efficiency ratio (FE<sub>R</sub>, unitless) assessed for pilot-scale 10 kW electrolyzers, while laboratory-scale reactors show 99.9% Faradaic efficiency. <sup>b</sup>Ratio of positive and negative charges at each stream.

A3. EDTA AND CaCO<sub>3</sub> DISSOLUTIONTable A2. Time Required (in min) to Reach >95% Ca Extraction during the EDTA-Aided Calcite Dissolution for a System Where CaCO<sub>3</sub> (in mol) = 1.1 × EDTA (in mol)

pH	EDTA concentration (mmol/L)		
	2	20	200
6	16 min	3 min	23 min
8	29 min	15 min	63 min
10	51 min	25 min	94 min

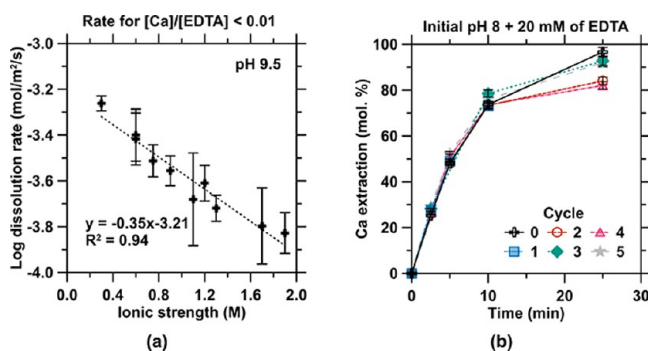


Figure A3. (a) Dissolution rate of calcite as a function of the solution's ionic strength for a starting pH of 9.5. (b) Performance of the recovered EDTA in chelating Ca extracted from calcite (CaCO<sub>3</sub>) compared to "pristine" AR-grade EDTA over 5 cycles of use and recovery.

## A4. MEMBRANE SCREENING AND PERFORMANCE

The NF membranes' performance were assessed on the basis of: water recovery, normalized permeate flux, observed

rejection, solute separation, solute mass transfer coefficient,<sup>57</sup> concentration polarization modulus,<sup>57</sup> Donnan partition coefficient in the case of monovalent permeation (NaHCO<sub>3</sub>) in the presence of highly impermeable charged organic molecules (Ca-EDTA<sup>2-</sup>),<sup>91,92</sup> real rejection, and pressure balance at increasing water recovery using the following equations:

$$Y_j = \frac{V_{\text{Permeate},j}}{V_{\text{Feed},0}} \quad (\text{A10})$$

$$\dot{V}_{\text{Permeate},j} = \frac{\Delta V_{\text{Permeate},j}}{A_m \Delta t_j \Delta P} \quad (\text{A11})$$

$$R_{\text{obs},x_{i,j}} = 1 - \frac{[x_i]_{\text{Permeate},j}}{[x_i]_{\text{Feed},j}} \quad (\text{A12})$$

$$\text{Sep}_{x_{i,j}} = \frac{m_{x_i, \text{Permeate},j}}{m_{x_i, \text{Initial},j}} \quad (\text{A13})$$

$$k_{x_{i,j}} = \frac{Sh_{x_{i,j}} D_{x_i}}{d_h} \quad (\text{A14})$$

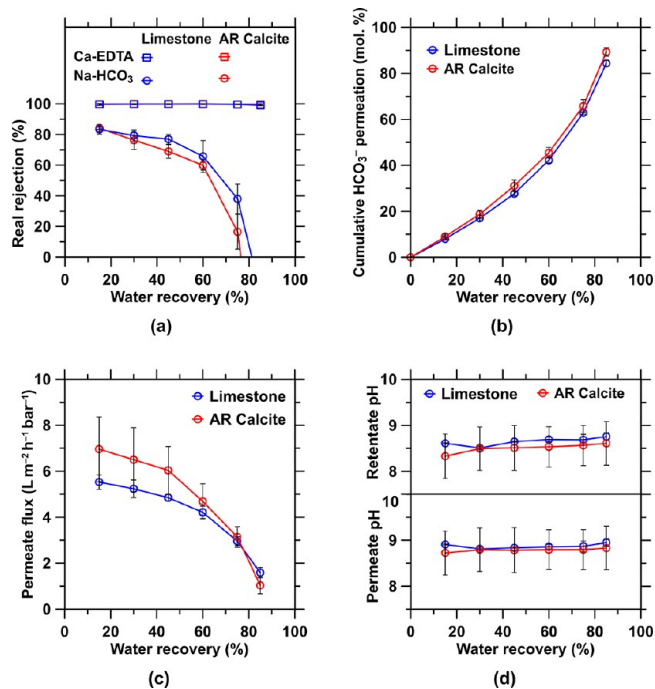
$$\text{CP}_{x_{i,j}} = \exp\left(\frac{v_{\text{Permeate},j}}{k_{x_{i,j}}}\right) \quad (\text{A15})$$

$$\beta_j = \sqrt{1 + \frac{\nu_{\text{Ca-EDTA}} [\text{Ca-EDTA}]_{\text{Feed},j}}{[\text{NaHCO}_3]_{\text{Feed},j}}} \quad (\text{A16})$$

$$R_{\text{real},x_{i,j}} = 1 - \frac{[x_i]_{\text{Permeate},j}}{\beta_j \text{CP}_{x_{i,j}} [x_i]_{\text{Feed},j}} \quad (\text{A17})$$

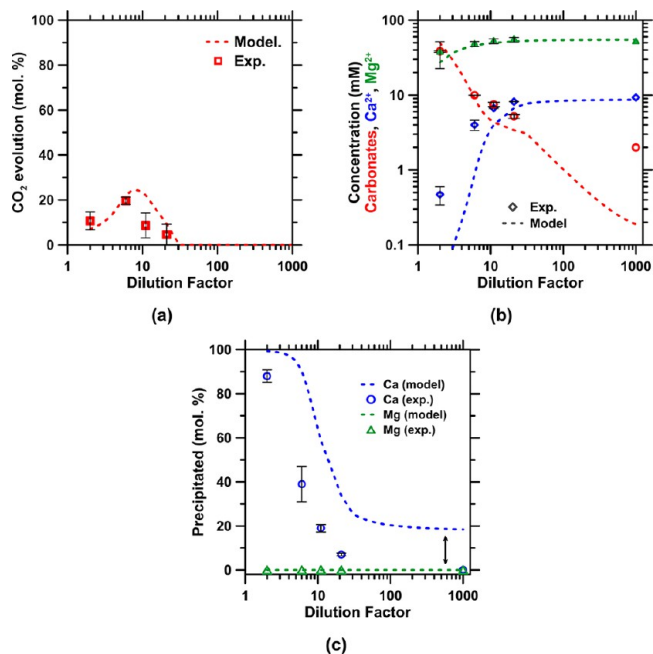
$$\Delta P_j = \Delta \pi_j + \Delta P_{x,j} + \frac{J_{w,j}}{A} \quad (\text{A18})$$

where  $V$  is the volume (m<sup>3</sup>) at water recovery  $j$  (%) or initial condition 0,  $A_m$  is the membrane active area (m<sup>2</sup>),  $\Delta t$  is the elapsed time (s),  $\Delta P$  is the applied hydraulic pressure (Pa),  $x_i$  is species  $x_i$ ,  $m_{x_i}$  is the mass of species  $x_i$ ,  $Sh$  is the Sherwood number (dimensionless),  $D_{x_i}$  is the diffusion coefficient of species  $x_i$  (m<sup>2</sup>/s),  $d_h$  is the hydraulic diameter (m),  $v_{\text{Permeate}}$  is the permeate flow velocity (m/s),  $v_i$  is the number of charged groups of species  $i$  (unitless),  $[x_i]$  is the concentration of species  $x_i$  (M),  $\Delta P_j$  is the applied hydraulic pressure,  $\Delta \pi$  is the transmembrane osmotic pressure (Pa),  $\Delta P_x$  is the cross-flow frictional pressure loss (Pa),  $J_w$  is the water flux (m<sup>3</sup>/s·m<sup>2</sup>), and  $A$  is the intrinsic water permeability (m<sup>3</sup>/s·m<sup>2</sup>·Pa).



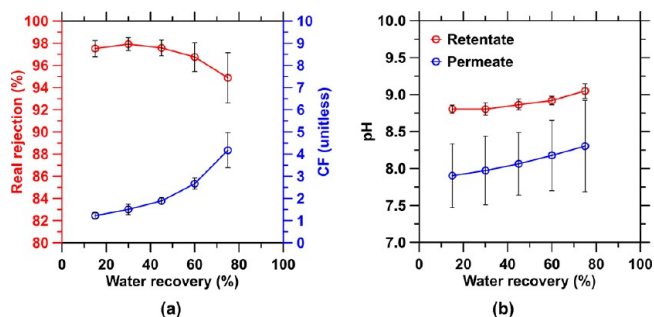
**Figure A4.** Performance of the XN45 membrane on single-stage NF with a pH 8 Ca-EDTA/Na-HCO<sub>3</sub> solution system as a function of water recovery comparing AR-grade calcite and natural limestone feedstocks: (a) Ca-EDTA and Na-HCO<sub>3</sub> real rejections; (b) profile of the cumulative HCO<sub>3</sub><sup>-</sup> permeation; (c) normalized permeate flux; (d) pH in the streams.

## A5. PROCESS-WATER RECYCLING AND OCEAN CARBON STORAGE



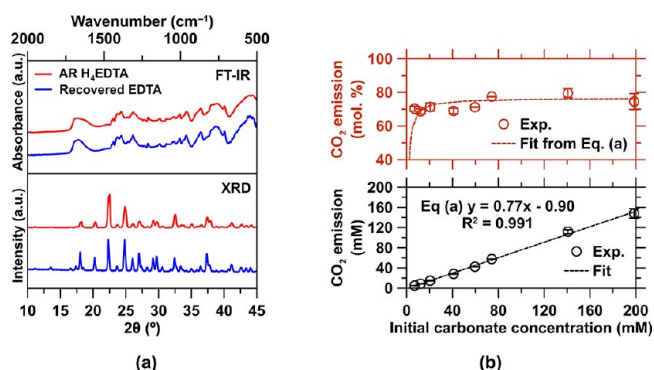
**Figure A5.** Effect of discharging a pH 9 stream containing 100 mmol/L aqueous Na-HCO<sub>3</sub> into seawater as a function of the considered dilution factor (the lines are thermodynamically modeled, and the points were acquired experimentally): (a) the carbonate evolution (as CO<sub>2</sub>), (b) the concentration of Mg, Ca, and the carbonate species, and (c) the amount of Ca and Mg precipitated, highlighting the

formation of calcium carbonate and the absence of hydrated magnesium carbonate formation in low dilution condition. The arrow indicates that the model fails to accurately represent the natural supersaturated state of seawater.

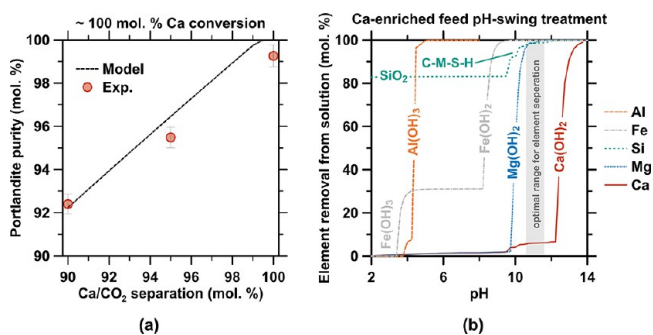


**Figure A6.** Performance of the NF90 NF membrane in Step 2a-ii on a Na-HCO<sub>3</sub>-containing solution from the previous separation Step 2a-i: (a) instantaneous Na-HCO<sub>3</sub> real rejection and concentration factor (CF) in the retentate stream; (b) pH in the streams.

## A6. EDTA RECOVERY



**Figure A7.** (a) XRD and FT-IR normalized patterns of the recovered EDTA precipitate and AR-grade H<sub>4</sub>EDTA. (b) Conservative estimate of the dissolved carbonate degassed from solution (as CO<sub>2</sub>) as a function of the initial carbonate concentration during the pH-swing from pH 8–10 to pH 2. No EDTA is present in the system, which removes the (low) dilution effect induced by EDTA titration.

A7. CA(OH)<sub>2</sub> ELECTROLYTIC PRECIPITATION

**Figure A8.** (a) Comparison between the experimental and modeled portlandite purity at  $\sim 100\%$  Ca conversion for different Ca/CO<sub>2</sub> separation values. (b) Contaminants (Al, Fe, Si, and Mg) removed from the Ca-enriched feed by precipitation of hydroxides and hydrated solids. SiO<sub>2</sub> is amorphous silica, and C-M-S-H is a calcium and magnesium containing silicate hydrate phase.

## A8. CONFIGURATION-SPECIFIC PROCESS CONDITIONS AND CARBON, WATER, AND ENERGY INTENSITIES

## AUTHOR INFORMATION

## Corresponding Author

**Gaurav Sant** – Laboratory for the Chemistry of Construction Materials (LC2), Department of Civil and Environmental Engineering, Department of Civil and Environmental Engineering, California Nanosystems Institute (CNSI), and Department of Materials Science and Engineering, University of California, Los Angeles, California 90095, United States; [orcid.org/0000-0002-1124-5498](https://orcid.org/0000-0002-1124-5498); Email: [gsant@ucla.edu](mailto:gsant@ucla.edu)

## Authors

**Adriano Leão** – Laboratory for the Chemistry of Construction Materials (LC2), Department of Civil and Environmental Engineering, University of California, Los Angeles, California 90095, United States; Institute for Carbon Management (ICM), University of California, Los Angeles, California 90095, United States; [orcid.org/0000-0001-6743-8099](https://orcid.org/0000-0001-6743-8099)

**Marie Collin** – Laboratory for the Chemistry of Construction Materials (LC2), Department of Civil and Environmental Engineering, University of California, Los Angeles, California 90095, United States; Institute for Carbon Management (ICM), University of California, Los Angeles, California 90095, United States; [orcid.org/0000-0002-0571-5019](https://orcid.org/0000-0002-0571-5019)

**Swarali Ghodkhande** – Laboratory for the Chemistry of Construction Materials (LC2), Department of Civil and Environmental Engineering, University of California, Los Angeles, California 90095, United States; Institute for Carbon Management (ICM), University of California, Los Angeles, California 90095, United States

**Arnaud Bouissonnié** – Laboratory for the Chemistry of Construction Materials (LC2), Department of Civil and

**Table A3.** Summary of the Selected Main Process Conditions and the Achieved Efficiencies at Ambient (*p*, *T*) Conditions

step	item	achieved efficiency (%)	general conditions	configuration	configuration-specific conditions	CO <sub>2</sub> degassing (mol. %)	process-water demand (t/t <sub>Ca(OH)<sub>2</sub></sub> )	energy intensity (MWh/t <sub>Ca(OH)<sub>2</sub></sub> )
0	electrochemical acid and base production	90 <sup>a</sup>	optimal current-to-flow rate ratio for low energy intensity	C1		0	315	4.18
				C2, C3		0	315	4.07
1	Ca extraction	100	initial [EDTA] = 100 mmol/L, [Ca]/[EDTA] ≥ 1	C1	initial pH = 9.5	0	(135) <sup>b</sup>	(2.51) <sup>b</sup>
2a	Ca/CO <sub>2</sub> separation	98–99	XN45 membrane, 8 < pH < 10, 85% water recovery	C2, C3	initial pH = 9.0	$\sim 1.0$	(135) <sup>b</sup>	(2.44) <sup>b</sup>
				C1	double-stage separation, minimal water recycling	0	115	0.45
				C2	single-stage separation, minimal water recycling	0	0	0.28
C3	single-stage separation, maximal water recycling	0	0	0.96				
2b	EDTA recovery	>99.9	tetra-protonation of EDTA, analyte pH < 1	C1		<1.5	(180) <sup>b</sup>	<sup>c</sup>
				C2, C3		$\sim 11.6$	(180) <sup>b</sup>	<sup>c</sup>
3	Ca(OH) <sub>2</sub> precipitation	55–90	[Ca] > 350 mmol/L	C1, C2, C3		0	0	(1.67) <sup>b</sup>
	additional energy intensity from seawater softening			C1				0.13
				C2, C3				0.10

<sup>a</sup>At scale (10 kW pilot plant), while laboratory-scale reactors show 99.9% Faraday efficiency. <sup>b</sup>Water or energy intensity already encompassed by Step 0. <sup>c</sup>Energy intensity already accounted for in Step 1, as acid and base are coproduced stoichiometrically.

*Environmental Engineering, University of California, Los Angeles, California 90095, United States; Institute for Carbon Management (ICM), University of California, Los Angeles, California 90095, United States; [orcid.org/0000-0003-4590-5631](https://orcid.org/0000-0003-4590-5631)*

**Xin Chen** – *Laboratory for the Chemistry of Construction Materials (LC2), Department of Civil and Environmental Engineering, University of California, Los Angeles, California 90095, United States; Institute for Carbon Management (ICM), University of California, Los Angeles, California 90095, United States; Equatic Inc., Los Angeles, California 90402, United States; [orcid.org/0000-0003-3273-4431](https://orcid.org/0000-0003-3273-4431)*

**Benjamin Malin** – *Laboratory for the Chemistry of Construction Materials (LC2), Department of Civil and Environmental Engineering, University of California, Los Angeles, California 90095, United States; Institute for Carbon Management (ICM), University of California, Los Angeles, California 90095, United States*

**Yiming Liu** – *Institute for Carbon Management (ICM), University of California, Los Angeles, California 90095, United States; [orcid.org/0000-0003-4761-5531](https://orcid.org/0000-0003-4761-5531)*

**Geanna Hovey** – *Laboratory for the Chemistry of Construction Materials (LC2), Department of Civil and Environmental Engineering, University of California, Los Angeles, California 90095, United States; Institute for Carbon Management (ICM), University of California, Los Angeles, California 90095, United States*

**Jagannathan Govindhakannan** – *Laboratory for the Chemistry of Construction Materials (LC2), Department of Civil and Environmental Engineering, University of California, Los Angeles, California 90095, United States; Institute for Carbon Management (ICM), University of California, Los Angeles, California 90095, United States*

**Erika La Plante** – *Institute for Carbon Management (ICM), University of California, Los Angeles, California 90095, United States; Department of Materials Science and Engineering, University of California, Davis, California 95616, United States; [orcid.org/0000-0002-5273-9523](https://orcid.org/0000-0002-5273-9523)*

**David Jassby** – *Institute for Carbon Management (ICM), University of California, Los Angeles, California 90095, United States; Department of Civil and Environmental Engineering and California Nanosystems Institute (CNSI), University of California, Los Angeles, California 90095, United States; [orcid.org/0000-0002-2133-2536](https://orcid.org/0000-0002-2133-2536)*

**Torben Gädt** – *Department of Chemistry, Technical University of Munich, Garching 85747, Germany; [orcid.org/0000-0001-7940-5403](https://orcid.org/0000-0001-7940-5403)*

**Lorenzo Corsini** – *Equatic Inc., Los Angeles, California 90402, United States; [orcid.org/0000-0002-8077-6559](https://orcid.org/0000-0002-8077-6559)*

**Dante Simonetti** – *Institute for Carbon Management (ICM), University of California, Los Angeles, California 90095, United States; Department of Chemical and Biomolecular Engineering, University of California, Los Angeles, California 90095, United States; [orcid.org/0000-0002-5708-460X](https://orcid.org/0000-0002-5708-460X)*

**Fabian Rosner** – *Institute for Carbon Management (ICM), University of California, Los Angeles, California 90095, United States; Department of Civil and Environmental Engineering, University of California, Los Angeles, California 90095, United States*

Complete contact information is available at:

<https://pubs.acs.org/10.1021/acssuschemeng.4c03193>

## Author Contributions

#A.L. and M.C. contributed equally as first coauthors.

## Notes

The authors declare no competing financial interest.

## Biographies



**Adriano Souza Leão** is a Ph.D. researcher at UCLA working on cement decarbonization technologies. He received a B.Sc. in Civil Engineering from the State University of Feira de Santana, during which he was awarded a scholarship to attend Colorado State University and the University of California, Davis, as a visiting international student. He then worked as a building design engineer. He received a M.Sc. in Industrial Technology Management from the SENAI CIMATEC University Center where he worked as a researcher in environmental modeling focusing on the life cycle assessment of industrial processes.



**Marie Collin** is a Staff Scientist at the Technische Universität München. She received her Ph.D. in Material Science from the Université de Montpellier. She worked at UCLA as a Postdoctoral Fellow and a Staff Scientist focusing on cement decarbonization and element recovery technologies.



**Swarali Ghodkhande** is a Ph.D. researcher at UCLA where she works on cement decarbonization and element recovery technologies. She received a Dual Degree (B.Tech + M.Tech) from Indian Institute of Technology, Bombay.



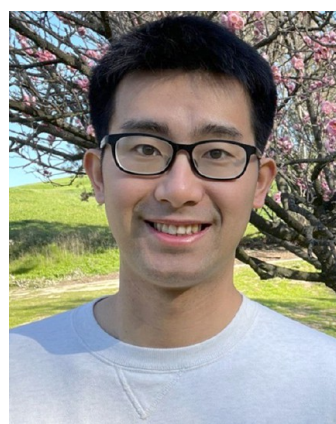
**Arnaud Bouissonnié** is a Staff R&D Engineer at UCLA's Institute for Carbon Management. He received his Ph.D. in geochemistry at the University of Strasbourg (France). His work focuses on topics related to electrochemical control of the mineral dissolution and precipitation process with a focus on the carbonate–silicate system.



**Xin Chen** is a Staff R&D Engineer at UCLA's Institute for Carbon Management. His works on electrochemical reactions are of relevance to the production, alteration, and corrosion of structural materials with applications in nuclear power generation, clean energy, and environmental technologies. He received his Ph.D. in Materials Engineering from the University of Illinois at Chicago.



**Benjamin Malin** worked as an Undergraduate Researcher at UCLA's Institute for Carbon Management. He is currently a B.S. student in Environmental Science at Washington University in St. Louis.



**Yiming Liu** earned his M.S. and Ph.D. in Civil and Environmental Engineering at UCLA and a B.S. in Environmental Engineering from Tsinghua University. He is currently a Rice Academy Postdoctoral Fellow at Rice University. His interests encompass interfacial and membrane processes for water treatment, resource recovery, and desalination.



**Geanna Hovey** is a Senior Process Development Engineer at UCLA's Institute for Carbon Management. She earned a B.A.Sc and M.A.Sc from the University of Waterloo and the University of Toronto, both in Environmental Engineering, and is a registered engineer in British Columbia. She has 10+ years of experience in process engineering, technology development, process scale-up, plant construction, and plant operations.



**Jagannathan Govindhakannan** is a Senior R&D Engineer at UCLA's Institute for Carbon Management. He received his Ph.D. in Chemical Engineering from Texas Tech University. Prior to UCLA, he was a Lead R&D Engineer at Honeywell UOP for 9 years. Govind's expertise is in the domains of technology scale-up, plant design, and chemical reaction engineering.



**Erika La Plante** is an Assistant Professor of Materials Science and Engineering at the University of California, Davis. She has a B.S. in Geology and a Ph.D. in Geochemistry (University of Illinois at Chicago) and previously held positions at UCLA and the University of Texas at Arlington. Erika applies her expertise in mineral dissolution and precipitation to discover new cements, extract critical metals, and sequester carbon dioxide.



**David Jassby** is a Professor of Civil and Environmental Engineering and Associate Director for Knowledge Discovery at the Institute for Carbon Management at UCLA. His research focuses on membrane separations, water treatment, electrochemistry, and resource recovery technologies.



**Torben Gädt** is a Professor of Chemistry at the Technical University of Munich where he holds the Chair in Construction Chemicals. His research focuses on cement, admixtures for concrete, and the chemistry of structural, inorganic materials.



**Lorenzo Corsini** is a scientist–entrepreneur with experience in building and scaling teams, technologies, and companies. He currently serves as the Principal Advisor of Equatic Inc. Previously, he cofounded and built PhagoMed, a biotech startup developing precision antibacterial drugs, which was sold to BioNTech in 2021. Prior to PhagoMed, he spent 9 years at the Boston Consulting Group. He has degrees in biochemistry and business administration and a Ph.D. in molecular biology.



**Dante Simonetti** is an Associate Professor of Chemical Engineering and Associate Director for Technology Translation at the Institute for Carbon Management at UCLA. He earned his B.S. and Ph.D. in Chemical Engineering from the University of Notre Dame and the University of Wisconsin—Madison, respectively. Prior to UCLA, he worked as an R&D Project Leader at Honeywell UOP. His research interests include reaction chemistry and engineering with a specific

focus on reducing the carbon footprint of industrial processes and energy generation.



**Fabian Rosner** is an Assistant Professor of Civil and Environmental Engineering at UCLA. His research focuses on renewable energy and chemical technologies that offer environmentally benign solutions to meet the growing demands for energy and consumer goods. Prior to UCLA, Fabian was a Postdoctoral Fellow at Lawrence Berkeley National Laboratory. He earned an M.S. and Ph.D. in Mechanical and Aerospace Engineering, specializing in thermal sciences, from the University of California, Irvine. He also earned a B.S. and M.S. in Chemical Engineering from the Technical University of Munich in Germany.



**Gaurav N. Sant** is a Professor and the Pritzker Endowed Chair in Sustainability at UCLA. He holds faculty appointments in the Departments of Civil and Environmental Engineering, Materials Science and Engineering, and California Nanosystems Institute. He is the Director of UCLA's Institute for Carbon Management, a cross-campus technology translation institute. He earned his B.S. (2006), M.S. (2007), and Ph.D. (2009), all in Civil Engineering, from Purdue University.

## ACKNOWLEDGMENTS

The authors acknowledge financial support provided by The Chan-Zuckerberg Initiative/Chan-Zuckerberg Initiative Foundation, The Grantham Foundation for the Protection of the Environment, The Anthony and Jeanne Pritzker Family Foundation, Shell Plc, Volkswagen/Audi, the U.S. Department of Energy's Advanced Research Projects Agency-Energy (AMENDER, DE-AR0001551; RECLAIM, DE-AR0001777), and UCLA's Institute for Carbon Management via the CAMELOT Technology Translation Initiative. The contents of this paper reflect the views and opinions of the authors, who are responsible for the accuracy of the datasets

presented herein and do not reflect the views and/or policies of the agency, nor do the contents constitute a specification, standard, or regulation.

## REFERENCES

- (1) De Brito, J.; Kurda, R. The Past and Future of Sustainable Concrete: A Critical Review and New Strategies on Cement-Based Materials. *Journal of Cleaner Production* **2021**, *281*, 123558.
- (2) Barcelo, L.; Kline, J.; Walenta, G.; Gartner, E. Cement and Carbon Emissions. *Mater. Struct* **2014**, *47* (6), 1055–1065.
- (3) Strunge, T.; Naims, H.; Ostovari, H.; Olfe-Kräutlein, B. Priorities for Supporting Emission Reduction Technologies in the Cement Sector - A Multi-Criteria Decision Analysis of CO<sub>2</sub> mineralisation. *Journal of Cleaner Production* **2022**, *340*, 130712.
- (4) Bustillo Revuelta, M. L. *Construction Materials*; Springer Textbooks in Earth Sciences, Geography and Environment; Springer International Publishing: Cham, Switzerland, 2021; pp 167–193; DOI: 10.1007/978-3-030-65207-4\_7.
- (5) FitzGerald, D.; Bourgaunt, G.; Vadenbo, C.; Sonderegger, T.; Symeonidis, A.; Fazio, S.; Mutel, C.; Müller, J.; Dellenbach, D.; Stoikou, N.; Baumann, D.; Clementi, M.; Ioannou, I.; Cirone, F.; Superti, V.; Beckert, P.; Treichel, A.; Kaarlela, O.; Kunde, S.; Valsasina, L.; Moreno Ruiz, E. Documentation of Changes Implemented in the Ecoinvent Database v3.10, 2023; <https://19913970.fs1.hubspotusercontent-na1.net/hubfs/19913970/Knowledge%20Base/Database/Releases/Change%20Report%20v3.10%20-%2020231214.pdf>.
- (6) Wernet, G.; Bauer, C.; Steubing, B.; Reinhard, J.; Moreno-Ruiz, E.; Weidema, B. The Ecoinvent Database Version 3 (Part I): Overview and Methodology. *Int. J. Life Cycle Assess* **2016**, *21* (9), 1218–1230.
- (7) Kellenberger, D.; et al. Life Cycle Inventories of Building Products. [https://db.ecoinvent.org/reports/07\\_BuildingProducts.pdf?area=463ee7e58cbf8](https://db.ecoinvent.org/reports/07_BuildingProducts.pdf?area=463ee7e58cbf8).
- (8) Madlool, N. A.; Saidur, R.; Rahim, N. A.; Kamalisarvestani, M. An Overview of Energy Savings Measures for Cement Industries. *Renewable and Sustainable Energy Reviews* **2013**, *19*, 18–29.
- (9) Afkhami, B.; Akbarian, B.; Beheshti, A. N.; Kakaee, A. H.; Shabani, B. Energy Consumption Assessment in a Cement Production Plant. *Sustainable Energy Technologies and Assessments* **2015**, *10*, 84–89.
- (10) Gielen, D.; Taylor, P. Indicators for Industrial Energy Efficiency in India. *Energy* **2009**, *34* (8), 962–969.
- (11) Madlool, N. A.; Saidur, R.; Hossain, M. S.; Rahim, N. A. A Critical Review on Energy Use and Savings in the Cement Industries. *Renewable and Sustainable Energy Reviews* **2011**, *15* (4), 2042–2060.
- (12) Olsson, J. A.; Miller, S. A.; Kneifel, J. D. A Review of Current Practice for Life Cycle Assessment of Cement and Concrete. *Resources, Conservation and Recycling* **2024**, *206*, 107619.
- (13) Campo, F. P.; Tua, C.; Biganzoli, L.; Pantini, S.; Grosso, M. Natural and Enhanced Carbonation of Lime in Its Different Applications: A Review. *Environmental Technology Reviews* **2021**, *10* (1), 224–237.
- (14) Andrew, R. M. Global CO<sub>2</sub> Emissions from Cement Production. *Earth Syst. Sci. Data* **2018**, *10* (1), 195–217.
- (15) DoE - U.S. Department of Energy. Pathway to Commercial Liftoff: Low-Carbon Cement, 2023. <https://liftoff.energy.gov/wp-content/uploads/2023/09/20230921-Pathways-to-Commercial-Liftoff-Cement.pdf>.
- (16) Benck, J. D.; Chiang, Y.-M.; Ellis, L. D.; Dominguez, K.; Layurova, M. Electrochemical Materials Production and Processing. Patent WO2022216741A1, October 13, 2022. <https://patents.google.com/patent/WO2022216741A1/en?q=wo2022%2f216741a1> (accessed 2023-11-06).
- (17) Benck, J. D.; Chiang, Y.-M.; Dominguez, K.; Ellis, L. D.; Jafari, K.; Layurova, M.; Macleod, A. Decarbonized Cement Blends. Patent WO2022204059A1, September 29, 2022. <https://patents>

google.com/patent/WO2022204059A1/en?oq=wo2022%2f204059a1 (accessed 2023-11-06).

(18) Finke, C. E.; Leandri, H. F. Process to Make Calcium Oxide or Ordinary Portland Cement from Calcium Bearing Rocks and Minerals. Patent US20220411328A1, December 29, 2022. <https://patents.google.com/patent/US20220411328A1/en?oq=US+2022%2f0411328+A1> (accessed 2023-11-06).

(19) FINKE, C.; Dry, M. J.; Kashyap, V.; Karumb, E. T.; Harvey-Costello, N.; Bresson, J. A.; Keller, M. J. Cementitious Material Production from Non-Limestone Material. Patent US20230036470A1, February 2, 2023. <https://patents.google.com/patent/US20230036470A1/en?q=brimstone+PROCESS+TO+MAKE+CALCIUM+OXIDE+OR+ORDINARY+PORTLAND+CEMENT+FROM+CALCIUM+BEARING+ROCKS+AND+MINERALS> (accessed 2023-11-06).

(20) Li, L.; Ling, T.-C.; Pan, S.-Y. Environmental Benefit Assessment of Steel Slag Utilization and Carbonation: A Systematic Review. *Science of The Total Environment* **2022**, *806*, 150280.

(21) Guo, J.; Bao, Y.; Wang, M. Steel Slag in China: Treatment, Recycling, and Management. *Waste Management* **2018**, *78*, 318–330.

(22) *Kinetics of Water–Rock Interaction*; Brantley, S. L., Kubicki, J. D., White, A. F., Eds.; Springer: New York, 2008; DOI: 10.1007/978-0-387-73563-4.

(23) Joint Research Centre, European Commission. Decarbonisation Options for the Cement Industry, 2023. [https://publications.jrc.ec.europa.eu/repository/bitstream/JRC131246/JRC131246\\_01.pdf](https://publications.jrc.ec.europa.eu/repository/bitstream/JRC131246/JRC131246_01.pdf).

(24) Arvidson, R. S.; Ertan, I. E.; Amonette, J. E.; Luttge, A. Variation in Calcite Dissolution Rates: *Geochim. Cosmochim. Acta* **2003**, *67* (9), 1623–1634.

(25) Coto, B.; Martos, C.; Peña, J. L.; Rodríguez, R.; Pastor, G. Effects in the Solubility of CaCO<sub>3</sub>: Experimental Study and Model Description. *Fluid Phase Equilib.* **2012**, *324*, 1–7.

(26) Lafon, G. M. Calcium Complexing with Carbonate Ion in Aqueous Solutions at 25°C and 1 atm. *Geochim. Cosmochim. Acta* **1970**, *34* (8), 935–940.

(27) Pearson, F. H.; McDonnell, A. J. Use of Crushed Limestone to Neutralize Acid Wastes. *J. Envir. Engrg. Div.* **1975**, *101* (1), 139–158.

(28) Plummer, L. N.; Parkhurst, D. L.; Wigley, M. L. Critical Review of the Kinetics of Calcite Dissolution and Precipitation. *ACS Symp. Ser.* **1979**, *93*, 537.

(29) Hart, J. R. Ethylenediaminetetraacetic Acid and Related Chelating Agents. *Ullmann's Encyclopedia of Industrial Chemistry*; Wiley-VCH Verlag GmbH & Co. KGaA: Weinheim, Germany, 2011; DOI: 10.1002/14356007.a10\_095.pub2.

(30) Zhu, Y.; Fan, W.; Zhou, T.; Li, X. Removal of Chelated Heavy Metals from Aqueous Solution: A Review of Current Methods and Mechanisms. *Science of The Total Environment* **2019**, *678*, 253–266.

(31) Dow. Chelation Chemistry: General Concepts of the Chemistry of Chelation, 2021. <https://www.dow.com/content/dam/dcc/documents/en-us/app-tech-guide/113/113-01388-01-chelation-chemistry-general-concepts-of-the-chemistry-of-chelation.pdf>.

(32) Fredd, C. N.; Fogler, H. S. The Influence of Chelating Agents on the Kinetics of Calcite Dissolution. *J. Colloid Interface Sci.* **1998**, *204* (1), 187–197.

(33) Oelkers, E. H.; Golubev, S. V.; Pokrovsky, O. S.; Bénézeth, P. Do Organic Ligands Affect Calcite Dissolution Rates? *Geochim. Cosmochim. Acta* **2011**, *75* (7), 1799–1813.

(34) Hassan, A. M.; Al-Hashim, H. S. Surface Charge Study of EDTA Interaction with Carbonate Rock during Chelating Agent Flooding. *J. Pet. Sci. Eng.* **2020**, *191*, 107163.

(35) La Plante, E. C.; Chen, X.; Bustillos, S.; Bouissonnie, A.; Traynor, T.; Jassby, D.; Corsini, L.; Simonetti, D. A.; Sant, G. N. Electrolytic Seawater Mineralization and the Mass Balances That Demonstrate Carbon Dioxide Removal. *ACS EST Eng.* **2023**, *3* (7), 955–968.

(36) La Plante, E. C.; Simonetti, D. A.; Wang, J.; Al-Turki, A.; Chen, X.; Jassby, D.; Sant, G. N. Saline Water-Based Mineralization Pathway for Gigatonne-Scale CO<sub>2</sub> Management. *ACS Sustainable Chem. Eng.* **2021**, *9* (3), 1073–1089.

(37) Llenas, L.; Ribera, G.; Martínez-Lladó, X.; Rovira, M.; De Pablo, J. Selection of Nanofiltration Membranes as Pretreatment for Scaling Prevention in SWRO Using Real Seawater. *Desalination and Water Treatment* **2013**, *51* (4–6), 930–935.

(38) Griko, Y. V. Energetics of Ca<sup>2+</sup>-EDTA Interactions: Calorimetric Study. *Biophys. Chem.* **1999**, *79* (2), 117–127.

(39) Zhou, D.; Zhu, L.; Fu, Y.; Zhu, M.; Xue, L. Development of Lower Cost Seawater Desalination Processes Using Nanofiltration Technologies — A Review. *Desalination* **2015**, *376*, 109–116.

(40) Ağtaş, M.; Yılmaz, Ö.; Dilaver, M.; Alp, K.; Koyuncu, İ. Hot Water Recovery and Reuse in Textile Sector with Pilot Scale Ceramic Ultrafiltration/Nanofiltration Membrane System. *Journal of Cleaner Production* **2020**, *256*, 120359.

(41) Chen, F.; Zhu, L.; Tang, J.; Li, D.; Yu, F.; Bai, F.; Ye, Z.; Cao, L.; Geng, N. A Pilot-Scale Nanofiltration-Ultrafiltration Integrated System for Advanced Drinking Water Treatment: Process Performance and Economic Analysis. *Processes* **2023**, *11* (5), 1300.

(42) Coutinho De Paula, E.; Martins, P. V.; Ferreira, I. C. D. M.; Amaral, M. C. S. Bench and Pilot Scale Performance Assessment of Recycled Membrane Converted from Old Nanofiltration Membranes. *Environmental Technology* **2020**, *41* (10), 1232–1244.

(43) Hilal, N.; Kochkodan, V.; Al Abdulgader, H.; Mandale, S.; Al-Jilil, S. A. A Combined Ion Exchange-Nanofiltration Process for Water Desalination: III. Pilot Scale Studies. *Desalination* **2015**, *363*, 58–63.

(44) Jadhav, S. V.; Marathe, K. V.; Rathod, V. K. A Pilot Scale Concurrent Removal of Fluoride, Arsenic, Sulfate and Nitrate by Using Nanofiltration: Competing Ion Interaction and Modelling Approach. *Journal of Water Process Engineering* **2016**, *13*, 153–167.

(45) Song, Y.; Li, T.; Zhou, J.; Pan, F.; Su, B.; Gao, C. Comprehensive Pilot-Scale Investigation of Seawater Nanofiltration Softening by Increasing Permeate Recovery with Recirculation. *Desalination and Water Treatment* **2016**, *57* (37), 17271–17282.

(46) Wadekar, S. S.; Hayes, T.; Lokare, O. R.; Mittal, D.; Vidic, R. D. Laboratory and Pilot-Scale Nanofiltration Treatment of Abandoned Mine Drainage for the Recovery of Products Suitable for Industrial Reuse. *Ind. Eng. Chem. Res.* **2017**, *56* (25), 7355–7364.

(47) El Fadil, A.; Verbeke, R.; Kyburz, M.; E. M. Aerts, P.; Vankelecom, I. F. J. From Academia to Industry: Success Criteria for Upscaling Nanofiltration Membranes for Water and Solvent Applications. *J. Membr. Sci.* **2023**, *675*, 121393.

(48) Van Der Bruggen, B.; Schaep, J.; Wilms, D.; Vandecasteele, C. Influence of Molecular Size, Polarity and Charge on the Retention of Organic Molecules by Nanofiltration. *J. Membr. Sci.* **1999**, *156* (1), 29–41.

(49) Mandale, S.; Jones, M. Interaction of Electrolytes and Non-Electrolytes in Nanofiltration. *Desalination* **2008**, *219* (1–3), 262–271.

(50) Dang, H. Q.; Price, W. E.; Nghiem, L. D. The Effects of Feed Solution Temperature on Pore Size and Trace Organic Contaminant Rejection by the Nanofiltration Membrane NF270. *Sep. Purif. Technol.* **2014**, *125*, 43–51.

(51) Simpson, A. E.; Kerr, C. A.; Buckley, C. A. The Effect of pH on the Nanofiltration of the Carbonate System in Solution. *Desalination* **1987**, *64*, 305–319.

(52) Chen, Q.-C.; Bang, Y.; Li, L.; Deng, H.-Y. High Flux and Antifouling Nanofiltration Membrane Modified by Ag@UiO-66-



- NH<sub>2</sub> and Its Application for Biphenol A Removal. *Advances in Polymer Technology* **2022**, *2022*, 1–17.
- (53) Richards, L. A.; Richards, B. S.; Corry, B.; Schäfer, A. I. Experimental Energy Barriers to Anions Transporting through Nanofiltration Membranes. *Environ. Sci. Technol.* **2013**, *47* (4), 1968–1976.
- (54) Balanyà, T.; Labanda, J.; Llorens, J.; Sabaté, J. Influence of Chemical Speciation on the Separation of Metal Ions from Chelating Agents by Nanofiltration Membranes. *Sep. Sci. Technol.* **2019**, *54* (1), 143–152.
- (55) Balanyà, T.; Labanda, J.; Llorens, J.; Sabaté, J. Separation of Metal Ions and Chelating Agents by Nanofiltration. *J. Membr. Sci.* **2009**, *345* (1–2), 31–35.
- (56) Oatley, D. L.; Llenas, L.; Pérez, R.; Williams, P. M.; Martínez-Lladó, X.; Rovira, M. Review of the Dielectric Properties of Nanofiltration Membranes and Verification of the Single Oriented Layer Approximation. *Adv. Colloid Interface Sci.* **2012**, *173*, 1–11.
- (57) Mulder, M. *Basic Principles of Membrane Technology*; Springer: Dordrecht, The Netherlands, 1996; DOI: 10.1007/978-94-009-1766-8.
- (58) Baker, R. W. *Membrane Technology and Applications*, 1st ed.; Wiley: New York, 2004; DOI: 10.1002/0470020393.
- (59) Di Palma, L.; Ferrantelli, P.; Merli, C.; Biancifiore, F. Recovery of EDTA and Metal Precipitation from Soil Flushing Solutions. *Journal of Hazardous Materials* **2003**, *103* (1–2), 153–168.
- (60) Lim, T.-T.; Chui, P.-C.; Goh, K.-H. Process Evaluation for Optimization of EDTA Use and Recovery for Heavy Metal Removal from a Contaminated Soil. *Chemosphere* **2005**, *58* (8), 1031–1040.
- (61) Goel, S.; Pant, K. K.; Nigam, K. D. P. Extraction of Nickel from Spent Catalyst Using Fresh and Recovered EDTA. *Journal of Hazardous Materials* **2009**, *171* (1–3), 253–261.
- (62) Lothenbach, B.; Kulik, D. A.; Matschei, T.; Balonis, M.; Baquerizo, L.; Dilnesa, B.; Miron, G. D.; Myers, R. J. Cemdata18: A Chemical Thermodynamic Database for Hydrated Portland Cements and Alkali-Activated Materials. *Cem. Concr. Res.* **2019**, *115*, 472–506.
- (63) Bard, A. J.; Faulkner, L. R. *Electrochemical Methods: Fundamentals and Applications*, 2nd ed.; Wiley: New York, 2001; p 833.
- (64) Dupont. Product Data Sheet: FilmTec™ NF90-400/34i Element, 2020. <https://www.dupont.com/content/dam/dupont/amer/us/en/water-solutions/public/documents/en/NF-FilmTec-NF90-400-34i-PDS-45-D01698-en.pdf>.
- (65) Ramdani, A.; Deratani, A.; Taleb, S.; Drouiche, N.; Lounici, H. Performance of NF90 and NF270 Commercial Nanofiltration Membranes in the Defluorination of Algerian Brackish Water. *DWT* **2021**, *212*, 286–296.
- (66) TriSep. TS40 NF for Purification, Separation, and Demineralization Data Sheet, 2021. <https://water-fluid-filtration.mann-hummel.com/content/dam/lse-wfs/product-related-assets/data-sheets/TS40-Flat-Sheet-Membrane.pdf>.
- (67) Dupont. Product Data Sheet: FilmTec™ NF270-440 Element, 2023. <https://www.dupont.com/content/dam/dupont/amer/us/en/water-solutions/public/documents/en/NF-FilmTec-NF270-440-PDS-45-D02827-en.pdf>.
- (68) Synder. NFW (TFC 300-500 Da): Sanitary NF Membrane, 2018. <https://synderfiltration.com/2014/wp-content/uploads/2018/11/NFW-TFC-300-500Da-Sanitary-Specsheet.pdf>.
- (69) TriSep. XN45 NF for Purification, Separation, and Demineralization Data Sheet, 2021. <https://water-fluid-filtration.mann-hummel.com/content/dam/lse-wfs/product-related-assets/data-sheets/XN45-Flat-Sheet-Membrane.pdf>.
- (70) TriSep. TS80 High Rejection NF Membrane, 2021. <https://water-fluid-filtration.mann-hummel.com/content/dam/lse-wfs/product-related-assets/data-sheets/TS80-Flat-Sheet-Membrane.pdf>.
- (71) TriSep. SB90 Cellulose Acetate (CA) NF Membrane, 2021. <https://water-fluid-filtration.mann-hummel.com/content/dam/lse-wfs/product-related-assets/data-sheets/SB90-Flat-Sheet-Membrane.pdf>.
- (72) Nadir. NP030 P “Nanofiltration” Membrane, 2022. <https://water-fluid-filtration.mann-hummel.com/content/dam/lse-wfs/product-related-assets/data-sheets/NP030-P-Flat-Sheet-Membrane%20change%20SLI%202022-03-08.pdf>.
- (73) Doebelin, N.; Kleeberg, R. Profex: A Graphical User Interface for the Rietveld Refinement Program BGMN. *J. Appl. Crystallogr.* **2015**, *48* (5), 1573–1580.
- (74) Rietveld, H. M. A Profile Refinement Method for Nuclear and Magnetic Structures. *J. Appl. Crystallogr.* **1969**, *2* (2), 65–71.
- (75) Bergmann, J.; Friedel, P.; Kleeberg, R. BGMN—a New Fundamental Parameters Based Rietveld Program for Laboratory X-Ray Sources, Its Use in Quantitative Analysis and Structure Investigations. *Commission on Powder Diffraction (IUCr)* **1998**, *20*, 5–8.
- (76) Kulik, D. A.; Wagner, T.; Dmytrieva, S. V.; Kosakowski, G.; Hingerl, F. F.; Chudnenko, K. V.; Berner, U. R. GEM-Selektor Geochemical Modeling Package: Revised Algorithm and GEMS3K Numerical Kernel for Coupled Simulation Codes. *Comput. Geosci* **2012**, 1–24.
- (77) Wagner, T.; Kulik, D. A.; Hingerl, F. F.; Dmytrieva, S. V. GEM-Selektor Geochemical Modeling Package: TSolMod Library and Data Interface for Multicomponent Phase Models. *Canadian Mineralogist* **2012**, *50* (5), 1173–1195.
- (78) Thoenen, T.; Hummel, W.; Berner, U.; Curti, E. *The PSINagra Chemical Thermodynamic Database 12/07*; Paul Scherrer Institut: Villigen, Switzerland, 2014; p PSI-Bericht Nr 14-04.
- (79) Hummel, W.; Berner, U.; Curti, E.; Pearson, F. J.; Thoenen, T. Nagra/PSI Chemical Thermodynamic Data Base 01/01. *Radiochim. Acta* **2002**, *90* (9–11), 805–813.
- (80) Johnson, J. W.; Oelkers, E. H.; Helgeson, H. C. SUPCRT92: A Software Package for Calculating the Standard Molal Thermodynamic Properties of Minerals, Gases, Aqueous Species, and Reactions from 1 to 5000 bar and 0 to 1000 °C. *Computers & Geosciences* **1992**, *18* (7), 899–947.
- (81) Helgeson, H. C.; Kirkham, D. H.; Flowers, G. C. Theoretical Prediction of the Thermodynamic Behavior of Aqueous Electrolytes by High Pressures and Temperatures; IV, Calculation of Activity Coefficients, Osmotic Coefficients, and Apparent Molal and Standard and Relative Partial Molal Properties to 600 Degrees C and 5 kb. *Am. J. Sci.* **1981**, *281* (10), 1249–1516.
- (82) Vollpracht, A.; Lothenbach, B.; Snellings, R.; Haufe, J. The Pore Solution of Blended Cements: A Review. *Mater. Struct* **2016**, *49* (8), 3341–3367.
- (83) Fournier, M.; Ull, A.; Nicoleau, E.; Inagaki, Y.; Odorico, M.; Frugier, P.; Gin, S. Glass Dissolution Rate Measurement and Calculation Revisited. *J. Nucl. Mater.* **2016**, *476*, 140–154.
- (84) Gin, S.; Beaudoux, X.; Angeli, F.; Jegou, C.; Godon, N. Effect of Composition on the Short-Term and Long-Term Dissolution Rates of Ten Glasses of Increasing Complexity from 3 to 30 Oxides. *J. Non-Cryst. Solids* **2012**, *358* (18–19), 2559–2570.
- (85) Sterlitech. Crossflow Filtration Handbook, 2018. [https://www.sterlitech.com/media/wysiwyg/Manual2018/Cross\\_Flow\\_Filtration\\_Handbook.pdf](https://www.sterlitech.com/media/wysiwyg/Manual2018/Cross_Flow_Filtration_Handbook.pdf).
- (86) Santafé-Moros, A.; Gozálviz-Zafrilla, J. M.; Lora-García, J. Experimental Simulation of Continuous Nanofiltration Processes by Means of a Single Module in Batch Mode. *Sep. Purif. Technol.* **2017**, *187*, 233–243.
- (87) Mohsen, M. S.; Jaber, J. O.; Afonso, M. D. Desalination of Brackish Water by Nanofiltration and Reverse Osmosis. *Desalination* **2003**, *157* (1–3), 167.
- (88) Labban, O.; Chong, T. H.; Lienhard, J. H. Design and Modeling of Novel Low-Pressure Nanofiltration Hollow Fiber Modules for Water Softening and Desalination Pretreatment. *Desalination* **2018**, *439*, 58–72.

- (89) Bouissonnié, A.; Daval, D.; Marinoni, M.; Ackerer, P. From Mixed Flow Reactor to Column Experiments and Modeling: Upscaling of Calcite Dissolution Rate. *Chem. Geol.* **2018**, *487*, 63–75.
- (90) Xu, J.; Fan, C.; Teng, H. H. Calcite Dissolution Kinetics in View of Gibbs Free Energy, Dislocation Density, and pCO<sub>2</sub>. *Chem. Geol.* **2012**, *322–323*, 11–18.
- (91) Perry, M.; Linder, C. Intermediate Reverse Osmosis Ultrafiltration (RO UF) Membranes for Concentration and Desalting of Low Molecular Weight Organic Solutes. *Desalination* **1989**, *71* (3), 233–245.
- (92) Gilron, J. Experimental Analysis of Negative Salt Rejection in Nanofiltration Membranes. *J. Membr. Sci.* **2001**, *185* (2), 223–236.
- (93) Schirg, P.; Widmer, F. Characterisation of Nanofiltration Membranes for the Separation of Aqueous Dye-Salt Solutions. *Desalination* **1992**, *89* (1), 89–107.
- (94) Glenthams Life Sciences Ltd.. EDTA Trisodium Salt Dihydrate; CAS RN: 150-38-9, GE9701 v3.0. Glenthams Life Sciences Ltd.: Corsham, U.K., 2024. <https://www.glenthams.com/en/products/product/GE9701/sds/?language=en> (accessed 2024-09-13).
- (95) Bachosz, K.; Smulek, W.; Zdart, J.; Jesionowski, T. A Novel Strategy for the Application of Levulinic Acid with Simultaneous NAD<sup>+</sup> Regeneration and Membrane Separation of Products. *Journal of Environmental Chemical Engineering* **2022**, *10* (6), 108703.
- (96) U.S. Environmental Protection Agency. National Recommended Water Quality Criteria—Aquatic Life Criteria Table, 2023. <https://www.epa.gov/wqc/national-recommended-water-quality-criteria-aquatic-life-criteria-table> (accessed 2024-09-13).
- (97) Koh, R. C. Y.; Brooks, N. H. Fluid Mechanics of Waste-Water Disposal in the Ocean. *Annu. Rev. Fluid Mech.* **1975**, *7* (1), 187–211.
- (98) Campos, C. J. A.; Morrissy, D. J.; Barter, P. Principles and Technical Application of Mixing Zones for Wastewater Discharges to Freshwater and Marine Environments. *Water* **2022**, *14* (8), 1201.
- (99) Intergovernmental Panel on Climate Change. Special Report on Carbon Dioxide Capture and Storage, 2005. [https://www.ipcc.ch/site/assets/uploads/2018/03/srccs\\_wholereport.pdf](https://www.ipcc.ch/site/assets/uploads/2018/03/srccs_wholereport.pdf).
- (100) Saraf, S.; Bera, A. Ocean Carbon Storage. *Advances and Technology Development in Greenhouse Gases: Emission, Capture and Conversion*; Elsevier, 2024; pp 67–89. DOI: 10.1016/B978-0-443-19067-4.00020-6.
- (101) Ochando-Pulido, J.; Martínez-Férez, A.; Stoller, M. Analysis of the Flux Performance of Different RO/NF Membranes in the Treatment of Agroindustrial Wastewater by Means of the Boundary Flux Theory. *Membranes* **2019**, *9* (1), 2.
- (102) Naidu, L. D.; Saravanan, S.; Chidambaram, M.; Goel, M.; Das, A.; Babu, J. S. C. Nanofiltration in Transforming Surface Water into Healthy Water: Comparison with Reverse Osmosis. *Journal of Chemistry* **2015**, *2015*, 1–6.
- (103) Bellona, C.; Drewes, J. E.; Oelker, G.; Luna, J.; Filteau, G.; Amy, G. Comparing Nanofiltration and Reverse Osmosis for Drinking Water Augmentation. *Journal - American Water Works Association* **2008**, *100* (9), 102–116.
- (104) Cipolletta, G.; Lancioni, N.; Akyol, Ç.; Eusebi, A. L.; Fatone, F. Brine Treatment Technologies towards Minimum/Zero Liquid Discharge and Resource Recovery: State of the Art and Techno-Economic Assessment. *Journal of Environmental Management* **2021**, *300*, 113681.
- (105) Ludwig-Böllow-Systemtechnik. The Hydrogen and Fuel Cell Information System, 2023. <http://www.h2data.de/> (accessed 2024-09-13).
- (106) Yuan-Hu, L.; Kim, J.; Lee, S.; Kim, G.; Han, H. Efficiency Improvement of a Fuel Cell Cogeneration Plant Linked with District Heating: Construction of a Water Condensation Latent Heat Recovery System and Analysis of Real Operational Data. *Applied Thermal Engineering* **2022**, *201*, 117754.
- (107) Zhao, D.; Qiu, L.; Song, J.; Liu, J.; Wang, Z.; Zhu, Y.; Liu, G. Efficiencies and Mechanisms of Chemical Cleaning Agents for Nanofiltration Membranes Used in Produced Wastewater Desalination. *Science of The Total Environment* **2019**, *652*, 256–266.
- (108) Gardarsdottir, S.; De Lena, E.; Romano, M.; Roussanaly, S.; Voldsund, M.; Pérez-Calvo, J.-F.; Berstad, D.; Fu, C.; Anantharaman, R.; Sutter, D.; Gazzani, M.; Mazzotti, M.; Cinti, G. Comparison of Technologies for CO<sub>2</sub> Capture from Cement Production—Part 2: Cost Analysis. *Energies* **2019**, *12* (3), 542.
- (109) Imbabi, M. S.; Carrigan, C.; McKenna, S. Trends and Developments in Green Cement and Concrete Technology. *International Journal of Sustainable Built Environment* **2012**, *1* (2), 194–216.
- (110) U.S. Energy Information Administration. Electricity Data (2018–2023), 2024. <https://www.eia.gov/electricity/> (accessed 2024-09-13).
- (111) Wei, M.; McMillan, C. A.; De La Rue Du Can, S. Electrification of Industry: Potential, Challenges and Outlook. *Curr. Sustainable Renewable Energy Rep* **2019**, *6* (4), 140–148.
- (112) Uratani, J. M.; Griffiths, S. A Forward Looking Perspective on the Cement and Concrete Industry: Implications of Growth and Development in the Global South. *Energy Research & Social Science* **2023**, *97*, 102972.
- (113) Intergovernmental Panel on Climate Change. AR6 Synthesis Report: Climate Change 2023, 2023. <https://www.ipcc.ch/report/sixth-assessment-report-cycle/> (accessed 2024-09-13).
- (114) Intergovernmental Panel on Climate Change. Buildings. *Climate Change 2022—Mitigation of Climate Change*; Cambridge University Press, 2023; pp 953–1048. DOI: 10.1017/9781009157926.011.
- (115) Despotou, E.; Shtiza, A.; Schlegel, T.; Verhelst, F. Literature Study on the Rate and Mechanism of Carbonation of Lime in Mortars/Literaturstudie Über Mechanismus Und Grad Der Karbonatisierung von Kalkhydrat Im Mörtel: Literature Study on the Rate and Mechanism of Carbonation of Lime in Mortars/Literaturstudie Über Mechanismus Und Grad Der Karbonatisierung von Kalk. *Mauerwerk* **2016**, *20* (2), 124–137.
- (116) Prentice, D.; Mehdipour, I.; Falzone, G.; Raab, S.; Simonetti, D.; Sant, G. Field Demonstration of the Reversa™ Mineral Carbonation Process Using Coal and Natural Gas Flue Gas Streams. In *REWAS 2022: Developing Tomorrow's Technical Cycles (Vol. 1)*; Lazou, A., Daehn, K., Fleuriault, C., Gökelman, M., Olivetti, E., Meskers, C., Eds.; The Minerals, Metals & Materials Series; Springer International Publishing: Cham, Switzerland, 2022; pp 589–594. DOI: 10.1007/978-3-030-92563-5\_62.
- (117) Falzone, G.; Mehdipour, I.; Neithalath, N.; Bauchy, M.; Simonetti, D.; Sant, G. New Insights into the Mechanisms of Carbon Dioxide Mineralization by Portlandite. *AIChE J.* **2021**, *67* (5). DOI: 10.1002/aic.17160.
- (118) Battaglia, G.; Romano, S.; Raponi, A.; Marchisio, D.; Ciofalo, M.; Tamburini, A.; Cipollina, A.; Micale, G. Analysis of Particles Size Distributions in Mg(OH)<sub>2</sub> Precipitation from Highly Concentrated MgCl<sub>2</sub> Solutions. *Powder Technol.* **2022**, *398*, 117106.
- (119) Vrana, L. M. Calcium and Calcium Alloys. In *Kirk–Othmer Encyclopedia of Chemical Technology*; John Wiley & Sons Inc.: Hoboken, NJ, 2001. DOI: 10.1002/0471238961.0301120308090202.a01.pub2.
- (120) Hosein, I. D. The Promise of Calcium Batteries: Open Perspectives and Fair Comparisons. *ACS Energy Lett.* **2021**, *6* (4), 1560–1565.
- (121) Stievano, L.; De Meatza, I.; Bitenc, J.; Cavallo, C.; Brutti, S.; Navarra, M. A. Emerging Calcium Batteries. *J. Power Sources* **2021**, *482*, 228875.
- (122) Royal Society of Chemistry. Periodic Table: Calcium, 2023. <https://www.rsc.org/periodic-table/element/20/calcium> (accessed 2024-09-13).
- (123) Trinkunaitė-Felsen, J.; Žalga, A.; Kareiva, A. Characterization of Naturally Derived Calcium Compounds Used in Food Industry. *CHEMIJA* **2012**, *23* (2), 76–85.

(124) Khan, M. A.; Reddy, I. K. Calcium Phosphate in Pharmaceutical Product Development. In *Calcium Phosphates in Biological and Industrial Systems*; Amjad, Z., Ed.; Springer USA: Boston, MA, 1998; pp 303–323. DOI: 10.1007/978-1-4615-5517-9\_13.

(125) Mititelu, M.; Stanciu, G.; Drăgănescu, D.; Ioniță, A. C.; Neacșu, S. M.; Dinu, M.; Stefan-van Staden, R.-I.; Moroșan, E. Mussel Shells, a Valuable Calcium Resource for the Pharmaceutical Industry. *Marine Drugs* **2022**, *20* (1), 25.

(126) Carella, F.; Degli Esposti, L.; Adamiano, A.; Iafisco, M. The Use of Calcium Phosphates in Cosmetics, State of the Art and Future Perspectives. *Materials* **2021**, *14* (21), 6398.

(127) Intergovernmental Panel on Climate Change. Annex III: Technology-Specific Cost and Performance Parameters, 2014. [https://www.ipcc.ch/site/assets/uploads/2018/02/ipcc\\_wg3\\_ar5\\_annex-iii.pdf](https://www.ipcc.ch/site/assets/uploads/2018/02/ipcc_wg3_ar5_annex-iii.pdf).

(128) BBC. Climate Change: The Massive CO<sub>2</sub> Emitter You May Not Know About. 2018. <https://www.bbc.com/news/science-environment-46455844> (accessed 2024-09-13).

(129) McKinsey & Company. Laying the Foundation for Zero-Carbon Cement. 2020. <https://www.mckinsey.com/industries/chemicals/our-insights/laying-the-foundation-for-zero-carbon-cement> (accessed 2024-09-13).

### ■ NOTE ADDED AFTER ASAP PUBLICATION

The version of this paper that was published ASAP October 10, 2024, contained an error in the exponent of eq 5. The corrected version was reposted to the Web October 28, 2024.